Univerzita Karlova v Praze

Přírodovědecká fakulta

Studijní program: Biologie

Studijní obor: Buněčná a vývojová biologie

Bc. Martin Petr

Nuclear myosin 1 and its role in the regulation of plasma membrane tension

Jaderný myosin 1 a jeho role v regulaci tenze cytoplazmatické membrány

Diplomová práce

Školitel: prof. RNDr. Pavel Hozák, DrSc.

Praha, 2014

Prohlášení

Prohlašuji, že jsem tuto diplomovou práci vypracoval samostatně a že jsem uvedl všechny použité informační zdroje a literaturu. Tato práce ani její podstatná část nebyla předložena k získání jiného nebo stejného akademického titulu.

V Praze, 5. května 2014

Martin Petr

First of all, I would like to thank my supervisor prof. Pavel Hozák for letting me participate in a project of my interest and for giving me the opportunity to work and think independently.

I am also incredibly grateful to Tomáš Venit, the coolest guy I have ever met. At the beginning I could not even hold a pipette properly and he taught me everything I know. I have once read that a career of every scientist is forever influenced by his first teacher and in that sense I could not have wished for anyone better. If I ever become a *real* scientist, it will be thanks to him.

I want to thank Janka Rohožková for endless discussions about science, life, universe and everything, properly supplemented by hectoliters of coffee and megatons of cake. It was awesome.

I would also like to thank Bětka Kalendová not only for her constant willingness to help, but also for her brutal honesty in times when it was necessary (and also when it was not! :)).

These are the people who had the greatest impact on my life in the lab. However, my special thanks go to *all* members of the lab – Ilona, Lívia, Pavel, Irina and others – thank you for everything! It was fun!

I am also indebted to Alexander Dulebo, Jakub Holáň and Jakub Malohlava for their assistance during AFM measurements and for sharing their valuable experience and advice.

Finally, my deepest gratitude goes to my parents and to Lenka, for their constant support and understanding and for always being there for me. I would not have achieved this without you.

Table of Contents

Abstract....5
List of abbreviations....7
1. Myosins....8
1.1 The myosin superfamily....8
1.2 Structure and functional characteristics of myosins....10
1.3 The myosin working cycle....10
1.4 Class I myosins....12
1.5 Myosin 1c isoforms....14
Nuclear myosin 1 (NM1)....15
Myosin 1c (Myo1c)....16
Isoform A....20
2. Atomic force microscopy....22
2.1 Basic principle of atomic force microscopy....22
2.2 Modes of AFM operation....24
Contact mode....24
Tapping mode....25
PeakForce tapping mode....25
2.3 Approach-retract cycle of the PeakForce tapping mode....26
2.4 Force-versus-indentation curves....27
3. Motivation and background....29
4. Aims....31
5. Materials and methods....32
Cell lines....32
Cell culture medium....33
Cell passaging....33
Antibodies....33
Immunofluorescence....33
Atomic force microscopy....34
Computing the Young's modulus of elasticity....35
Visualization of spatial distribution of membrane elasticity....36
Analysis of cell heights....37
Statistics....38
6. Results....39
Myosin 1c isoforms localize to the plasma membrane and cell periphery....39
NM1 has a similar localization pattern as Myo1c....42
Targeting of NM1 to the plasma membrane is PIP2-dependent....42
Loss of NM1 leads to a significantly higher membrane elasticity....44
High elasticity of rescued NM1 KO cells is partially reversed to WT phenotype....48
High elasticity of NM1 KO cells is uniform over the whole cell surface....50
Depletion of Myo1c isoforms in U2OS cells does not affect membrane properties....53
Knockout of NM1 has no effect on cell height....55
Membrane elasticity of NM1 KO cells shows a high degree of spatial homogeneity....56
Loss of NM1 has no detectable effect on cell shape or morphology....58
7. Discussion....62
8. Summary....69
References....70

Abstract

Myosin 1c (Myo1c) is a molecular motor involved in regulation of tension-gated ion channels, exocytosis, endocytosis, motility and other membrane-related events. Moreover, it acts as a dynamic linker between the cell membrane and cortical actin network, contributing to the maintenance of plasma membrane tension. In contrast, nuclear myosin 1 (NM1), an isoform of Myo1c, has been described only in the nucleus where it participates in various nuclear processes, including transcription or chromatin remodeling. However, although traditionally regarded as exclusively cytoplasmic or nuclear, all myosin 1c isoforms participate in nuclear functions and they are present in the cytoplasm as well. The main focus of this study was to characterize the functional significance of NM1 in the cytoplasm. We have found that NM1 localizes to plasma membrane and shows a uniform punctuated distribution with a high concentration at the cell periphery. Moreover, atomic force microscopy measurements of mouse NM1 KO fibroblasts revealed a significant increase in an overall plasma membrane elasticity in comparison to WT cells, indicating a disruption in the regulation of plasma membrane tension caused by the loss of NM1. Since a higher membrane elasticity and deformability is a characteristic marker of cancer cells, presumably increasing their metastatic potential, we suggest that deletion or mutation of the NM1 protein might lead to an increased susceptibility to metastatic cancer.

Keywords: myosin 1c, nuclear myosin 1, plasma membrane tension, cell elasticity, cortical actin cytoskeleton, membrane-cytoskeleton interaction, atomic force microscopy, AFM, Young's modulus

Abstrakt

Myosin 1c (Myo1c) je molekulární motor působící v regulaci mechanosenzitivních kanálů, exocytóze, endocytóze či motilitě buněk a přispívá také k udržování tenze cytoplazmatické membrány, kde funguje jako dynamická spojka mezi membránou a kortikálním aktinovým cytoskeletem. Jaderný myosin 1 (NM1), isoforma Myo1c, byl zatím detailně popsán pouze v jádře, kde se podílí například na procesu transkripce či remodelace chromatinu. Bylo ale zjištěno, že přestože byly oba proteiny tradičně považovány za čistě cytoplazmatické či jaderné, ve skutečnosti se na jaderných procesech podílejí všechny isoformy myosinu 1c a všechny jsou přítomny také v cytoplazmě. Cílem této práce bylo charakterizovat funkční význam NM1 v cytoplazmě. Zjistili jsme, že je NM1 lokalizován rovnoměrně na cytoplazmatické membráně a je silně koncentrován zejména na okrajích buněk. Měření na mikroskopu atomárních sil dále prokázalo významný nárůst v elasticitě plazmatické membrány NM1 knockout fibroblastů, což naznačuje narušení mechanismu regulujícího membránovou tenzi buněk v důsledku ztráty NM1. Jelikož je vyšší elasticita membrány a deformovatelnost charakteristickým znakem rakovinných buněk a pravděpodobně zvyšuje jejich metastatický potenciál, navrhujeme, že by delece nebo mutace v NM1 mohly vést k vyšší náchylnosti k metastázám.

Klíčová slova: myosin 1c, jaderný myosin 1, tenze cytoplazmatické membrány, elasticita buněk, kortikální aktinový cytoskelet, interakce membrána-cytoskelet, mikroskopie atomárních sil, AFM, Youngův modul

List of abbreviations

2D	two-dimensional
3D	three-dimensional
AA	amino acid
ADP	adenosine diphosphate
AFM	atomic force microscope/microscopy
ATP	adenosine triphosphate
DAPI	DNA-binding fluorescent stain
GLUT4	glucose transporter type 4
IQ	isoleucine/glutamine-rich region
Hz	hertz
kHz	kilohertz
kPa	kilopascal
KO	knockout
mRNA	messenger RNA
MPa	megapascal
Myo1c	myosin 1c–isoform C
MYO1C	gene encoding myosin 1c isoforms
Myo1c-isoA	myosin 1c–isoform A
Neph1	Nephrin-like protein
NM1	nuclear myosin 1; myosin 1c–isoform B
PFT	PeakForce tapping
PH	pleckstrin-homology
Pi	inorganic phosphate
PIP_2	phosphatidylinositol-4,5-bisphosphate
RNA	ribonucleic acid
S.D.	standard deviation
TH1	tail-homology 1
U2OS	human osteosarcoma cell-line
YM	Young's modulus of elasticity
WT	wild-type

1. Myosins

1.1 The myosin superfamily

Myosins are molecular motors that are able to hydrolyze ATP molecules and use the released energy to perform mechanical work in co-operation with actin microfilaments. Based on phylogenetic studies, they form a large superfamily of proteins divided into at least 35 classes and can be found across the entire eukaryotic domain with the exception of several metamonads and red algae (fig. 1.1) (Richards and Cavalier-Smith, 2005; Odronitz and Kollmar, 2007). In fact, mammalian genomes contain up to 40 different myosin genes (Foth et al., 2006), which reflects a wide range of cellular functions covered by these proteins.

Based on their structural features, myosins have been traditionally divided into two distinct groups, the so-called conventional and unconventional myosins. A fundamental characteristic of conventional myosins is their ability to assemble into bipolar filaments by interacting through their long coiled-coil tail domains (Hartman and Spundich, 2012). The first conventional myosin was discovered in the skeletal muscle and in 1954 it was found that the sliding of myosin and actin filaments in the sarcomeres provides a basis of muscle contraction (Huxley and Niedergerke, 1954; Huxley and Hanson, 1954). Since then, several other non-muscle myosin proteins have been discovered, all sharing the multimeric filamentous feature of conventional muscle myosins (McConnell and Tyska, 2010). The ability of conventional myosins to form bipolar thick filaments of co-operating molecular motors allows them to function in processes that require directed and co-ordinated force. Therefore, in addition to muscle contraction, conventional myosins have been shown to participate in other events, such as in tightening of the contractile ring during cytokinesis (Maupin et al., 1994) or neural growth cones motility (Bridgman et al., 2001). Today, muscle and non-muscle conventional myosins are grouped in the class II of the myosin superfamily and represent the largest class of myosin molecular motors (fig. 1.1, group Mhc) (Odronitz and Kollmar, 2007).

In contrast to conventional myosins, unconventional myosins function either as monomers or dimers and they do not form any kind of bipolar filaments (Hartman and Spundich, 2012). Since the discovery of the first unconventional myosin in 1973 (Pollard and Korn, 1973), a large number of unconventional myosins has been described and divided into

many different classes (Richards and Cavalier-Smith, 2005; Odronitz and Kollmar, 2007). They participate in a wide range of cellular processes, including intracellular transport (Vale, 2003), cell migration (Wang et al., 2003), maintenance of plasma membrane tension (Nambiar et al., 2009), regulation of actin dynamics and membrane protrusions (Nambiar et al., 2010), exocytosis (Schietroma et al., 2007) and endocytosis (Sokac et al., 2006) and others (Woolner and Bement, 2009; Hartman and Spudich, 2012).

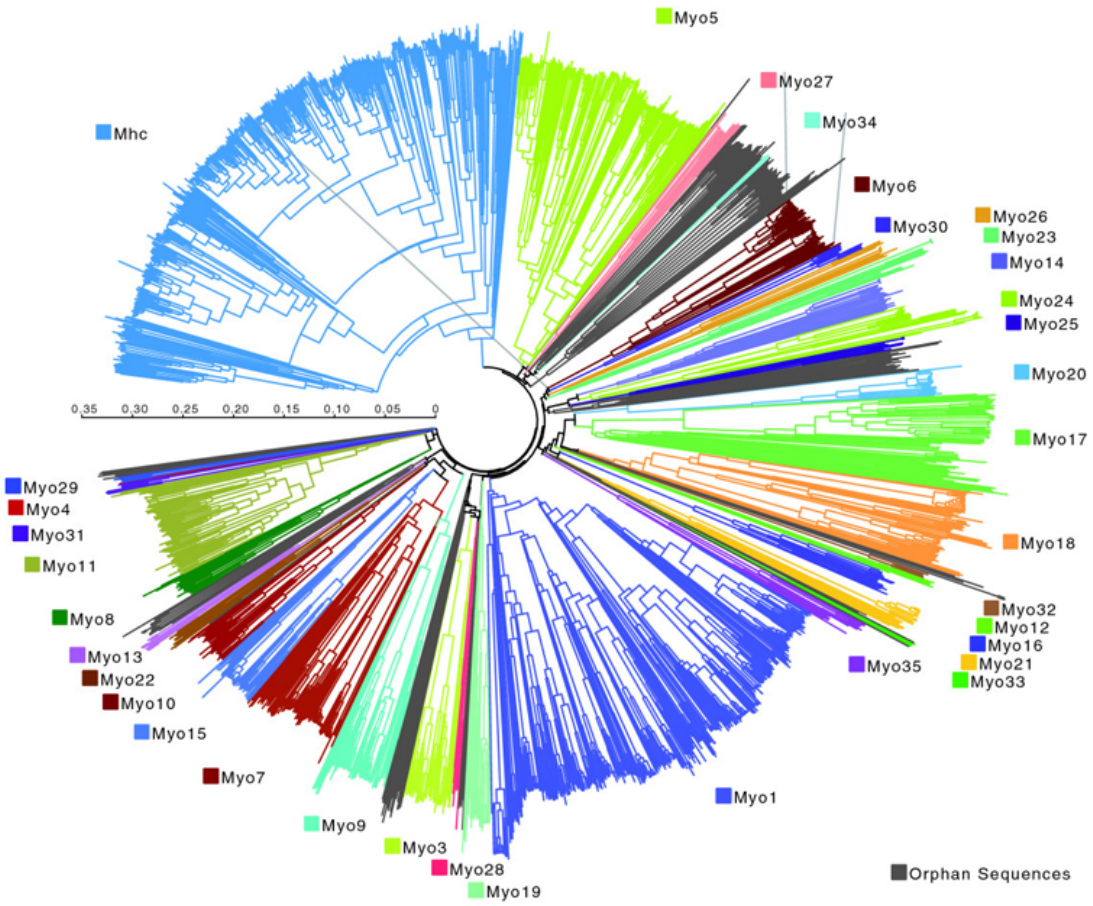

Figure 1.1. Phylogenetic tree of the myosin superfamily based on sequences of myosin motor domains. *Conventional myosins are grouped as Mhc. Figure was taken and adapted from Odronitz and Kollmar, 2007.*

1.2 Structure and functional characteristics of myosins

All members of the myosin superfamily share a three domain structure consisting of the head, neck and tail domain. The globular head domain, located in the N-terminal part of the protein, contains nucleotide-binding and actin-binding sites and has a highly evolutionary conserved protein sequence (Cope et al., 1996; Foth et al., 2006). In contrast, the C-terminal tail domains are highly divergent, allowing for the wide range of their functional variability (Hartman and Spundich, 2012), and they often form a coiled-coil structure of variable length (Syamaladevi et al., 2012). In conventional myosins, these coiled-coils serve as oligomerization sites, facilitating the formation of bipolar myosin filaments, increasing their apparent motor processivity (Ostap and Pollard, 1996). In unconventional myosins, the tail contains different domains that bind myosins to cargoes via various adaptor proteins, or target them to specific cellular location or function (Akhmanova and Hammer, 2010). The head domain and the tail domain are connected through an α-helical neck domain that serves as a lever arm, transferring and amplifying the force generated during the power stroke phase of the myosin working cycle (Uyeda et al., 1996; Warshaw et al. 2000). The neck domain contains a variable number of IQ motifs that serve as binding sites for calmodulin or calmodulin-like subunits, also known as myosin light chains, which form a tight grip around the IQ motifs in a calcium-dependent manner and regulate the myosin motor function (Houdusse et al., 2006). The maximum motor force depends on the overall stiffness of the lever arm. In the absence of calcium, the calmodulin light chains bind to the myosin neck domain, increase the stiffness and rigidity of the lever arm and allows it to transmit the force efficiently (Uyeda et al., 1996). Furthermore, it has been shown that the step size of a myosin motor is directly proportional to the length of the lever arm and, therefore, that the longer neck regions lead to more rapid movement (Warshaw et al. 2000; Purcell et al., 2002).

1.3 The myosin working cycle

The motor function of the acto-myosin complex relies on dramatic conformational changes in the myosin protein that influence its actin-binding affinity as it progresses through the ATPase working cycle. Specifically, myosin mechanical function is based on its ability to transform relatively small structural changes in its nucleotide-binding site into large conformational transitions in its actin-binding site and in their power-stroke generating neck domain (Fischer

et al., 2005). The basic principle of this working cycle, first proposed by Lymn and Taylor (Lymn and Taylor, 1971), is shared among all variants of myosin molecules and is schematically described in fig. 1.2 (De La Cruz and Ostap, 2004).

At the beginning of the myosin working cycle, a nucleotide is absent from the nucleotide-binding site and the myosin is tightly bound to actin in the so-called *rigor* state (Holmes and Geeves, 2000). The binding of an ATP molecule to myosin induces a conformational change in the actin-binding site (fig. 1.2, step 1), weakening its actin-binding affinity which leads to the rapid and irreversible dissociation of the acto-myosin complex (fig. 1.2, step 2). Following the myosin detachment, ATP is hydrolyzed into ADP and Pi (inorganic phosphate) which is accompanied by a conformational change in the neck domain (fig. 1.2, step 3), allowing myosin to rebind to the next actin molecule in a forward direction via the so-called recovery stroke (fig. 1.2 , step 4). In this stage, the acto-myosin complex is weakly associated and ADP + Pi still remain bound to the myosin head. The binding to actin induces a large conformational change leading to a large rotation of the myosin lever arm and causing the myosin to pull along the actin filament (Fischer et al., 2005). This force-generating power stroke of strongly bound myosin is coincident with the release of Pi (fig. 1.2, step 5) and leaves the myosin tightly bound to actin filament, ready for another cycle after the ADP is released from the nucleotide-binding pocket (fig. 1.2, step 6) (De La Cruz and Ostap, 2004).

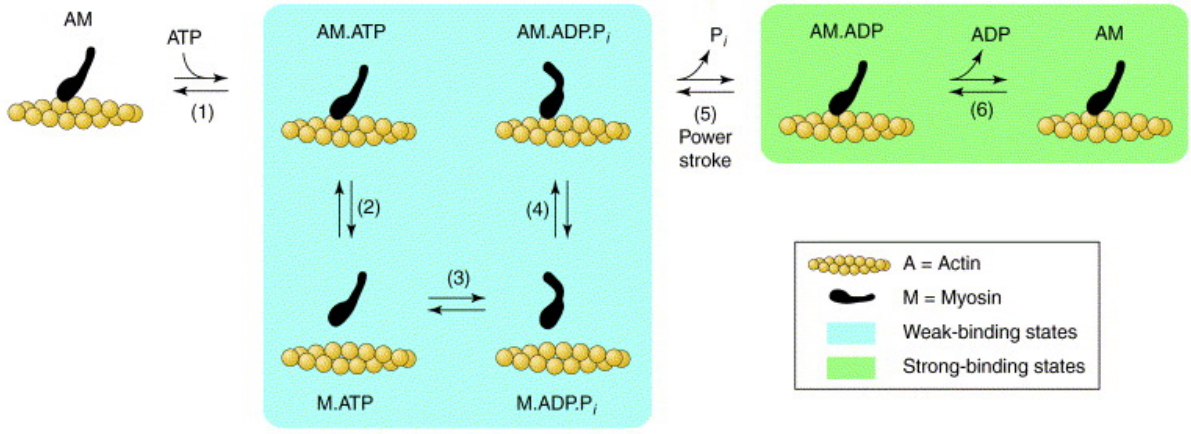

Figure 1.2. The myosin working cycle. *Blue and green frames indicate weak-binding and strong-binding states of myosin, respectively. Figure was taken and adapted from De La Cruz and Ostap, 2004.*

While the basic principle of the acto-myosin working cycle is shared by all myosins, each class differs in various functional parameters and kinetic properties, such as the rate of ATP hydrolysis, the velocity of the motor movement on an actin fiber or a duty ratio, which represents the fraction of time a particular motor protein spends strongly bound to a filament during its working cycle (Leibler and Huse, 1993).

The range of possible functions that an individual type of myosin can efficiently perform is largely dependent on these parameters. For example, in order to maintain an uninterrupted interaction with actin filaments to generate continuous force during muscle contraction, a low duty muscle myosins are required to form multimeric bundles of co-operating molecules. In contrast, a high duty myosin spends a large portion of its working cycle strongly bound to actin. Therefore, it is able to work efficiently as a single, long-distance cargo transporter (Leibler and Huse, 1993).

1.4 Class I myosins

Class I myosins are monomeric molecular motors that are ubiquitously present in a majority of eukaryotic organisms (Richards and Cavalier-Smith, 2005; Odronitz and Kollmar, 2007). There are eight different class I myosins in vertebrates and, like all other members of the myosin superfamily, they share a similar three-domain structure (fig. 1.3A) (McConnell and Tyska, 2010). Their head domain contains nucleotide-binding and actin-binding sites and their neck lever domain contains calmodulin-binding IQ motifs (fig. 1.3B). However, unlike other classes of myosins, the C-terminal tail of all class I myosins carries a unique tail-homology 1 (TH1) domain containing a pleckstrin homology (PH) motif which gives them an ability to bind to phospholipids, especially phosphatidyl inositol 4,5-bisphosphate (PIP_2) (Hokanson et al., 2006a; Hokanson et al., 2006b). Additionally, binding sites for PIP_2 and other phospholipids were discovered in calmodulin-binding IQ motifs, leading to a hypothesis that this is might represent an alternative mechanism of interaction with the plasma membrane (Hirono et al., 2004; Barylko et al., 2005).

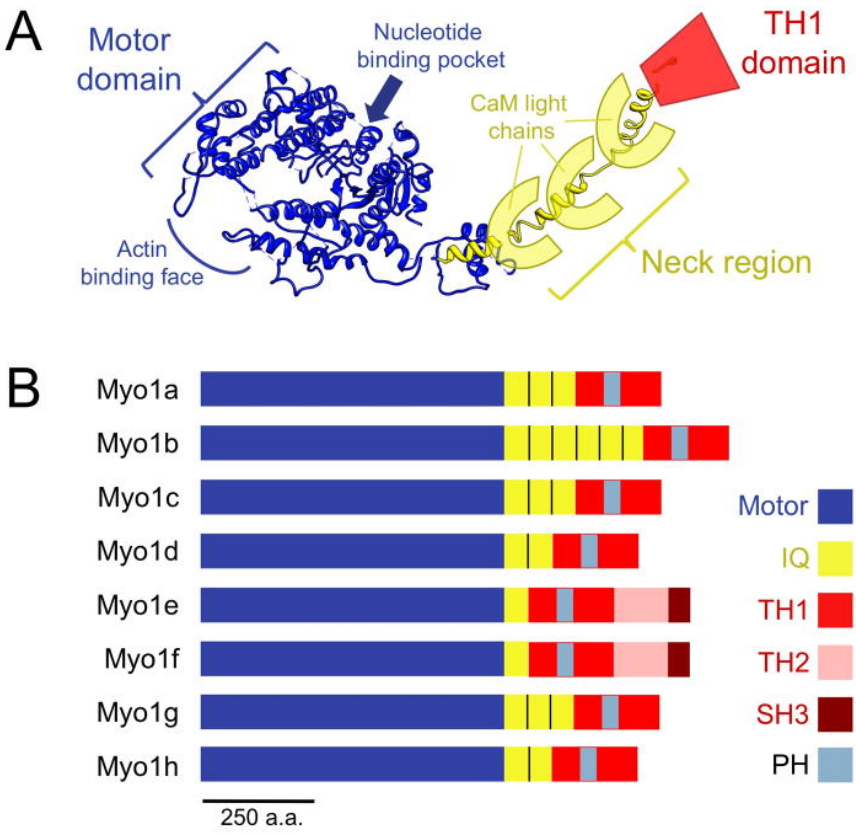

Figure 1.3. Structure of class I vertebrate myosins. ***(A)*** *Predicted three-dimensional structure of myosin 1a.* ***(B)*** *Schematic representation of domain structures of eight vertebrate class I myosins. It can be seen that Myo1a-h contain various interaction sites. IQ – isoleucine/glutamine-rich region, TH1/2 – C-terminal tail homology domains, SH3 – Src homology domain, PH – pleckstrin-homology domain. Figure was taken and adapted from McConnell and Tyska, 2010.*

All class I myosins are monomeric low-duty ratio molecular motors and, as such, they spend most of their working cycle only weakly attached or completely detached from actin filaments (McConnell and Tyska, 2010). Since they have a low rate of ATP turnover as well as a slow movement on actin filaments, this makes them unsuitable to function as long-distance transporters of cellular cargo (Ostap and Pollard, 1996). However, it has been shown that class I myosins have a unique ability to increase their duty ratio in response to forces exerted in direction opposing their movement (Laakso et al., 2008). Specifically, the power stroke of class I myosins occurs in two phases, where an initial movement of the lever arm, accompanied by the release of Pi, is followed by an additional swing of the lever arm, coincident with the ADP release (Veigel et al., 1999; Batters et al., 2004a; Batters et al.,

2004b). Therefore, since the ADP release is a rate-limiting step for detachment from an actin filament (Siemankowski et al., 1985), the resistance force exerted by an opposing load prevents the ADP release, thus prolonging the tight actin-bound state of the myosin and increasing its effective duty ratio from less than 20% up to 90%. Based on these observations, it has been proposed that these proteins act as molecular sensors of mechanical tension (Laakso et al., 2008). Moreover, since they have been shown to participate in the maintenance of plasma membrane tension, it has been suggested that class I myosins have regulatory roles in processes controlled by cell membrane tension such as endocytosis, exocytosis, cell motility or cell spreading (Nambiar et al., 2009; McConnell and Tyska, 2010; Diz-Muñoz et al., 2013).

1.5 Myosin 1c isoforms

Myosin 1c isoforms are gene products of the *MYO1C* gene, which is located on chromosome 11 in mice and on chromosome 17 in humans (Pestic-Dragovich et al., 2000). These proteins belong to the class I of the myosin superfamily and there are currently three isoforms known to be encoded by the *MYO1C* gene: myosin 1c–isoform A (Myo1c-isoA), myosin 1c–isoform B (also known as nuclear myosin 1, NM1) and myosin 1c–isoform C (myosin 1c, Myo1c). All three isoforms are expressed in humans, however, only two of them, NM1 and Myo1c, are expressed in mice. They result from alternatively spliced *MYO1C* transcripts which differ in the presence of unique starting exons E-3 (for Myo1c-isoA), E-2 (for Myo1c) and E-1 (for NM1), and carry alternative start codons (fig. 1.4). Therefore, at the protein level, all myosin 1c isoforms are very similar and they differ only by short N-terminal extensions of NM1 and Myo1c-isoA (fig. 1.4).

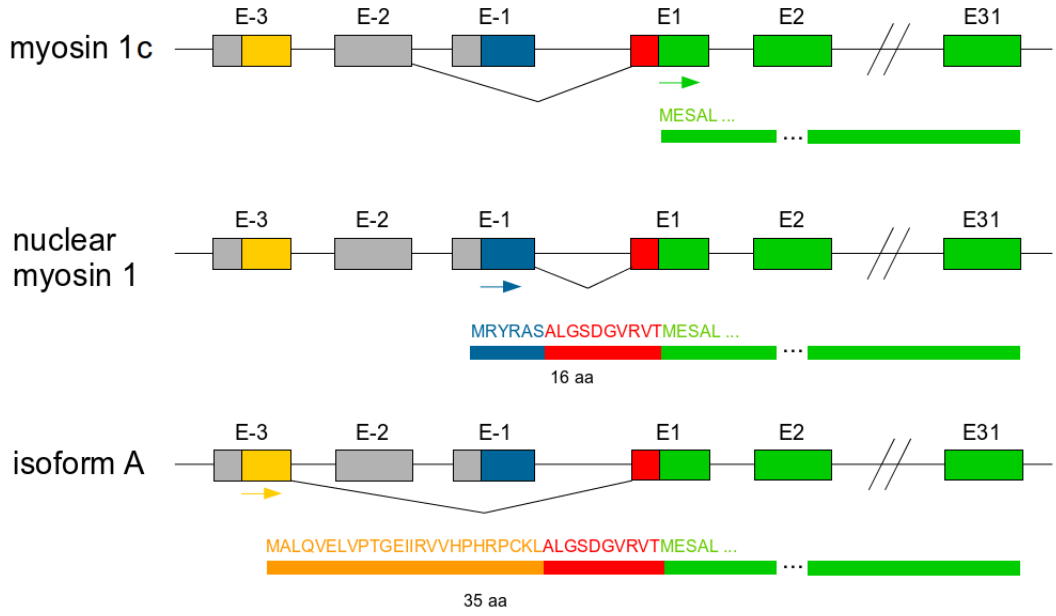

Figure 1.4. Structure of the* MYO1C *gene. *The gene encodes three isoforms, myosin 1c, nuclear myosin 1 and myosin 1c–isoform A. All three isoforms are expressed in humans, however, only two of them, NM1 and Myo1c, are expressed in mice. All isoforms result from an alternatively spliced transcripts which differ in the presence of unique starting exons (E-1, E-2, E-3) and carry alternative start codons (indicated by green, blue and orange arrows).*

Nuclear myosin 1 (NM1)

Nuclear myosin 1 (NM1) was the first molecular motor discovered in the cell nucleus (Nowak et al., 1997; Pestic-Dragovich et al., 2000). The NM1 mRNA results from an alternative splicing of the *MYO1C* transcript and it begins with NM1-specific exon -1 which carries an alternative translation start site. This start codon lies in frame with the downstream Myo1c-specific translation start site on the exon 1, shared by all myosin 1c isoforms, and results in a 16 amino acid N-terminal extension that separates NM1 from the shorter Myo1c isoform (fig. 1.4) (Pestic-Dragovich et al., 2000). NM1 is highly evolutionary conserved among vertebrate species and it is ubiquitously expressed in various mouse tissues with the exception of late stage spermatocytes (Kahle et al., 2007).

Since its discovery, a number of important nuclear functions of NM1 have been described. In the nucleolus, NM1 and actin physically associate with RNA polymerase I and are both involved in transcription of ribosomal genes (Fomproix and Percipalle, 2004; Philimonenko et al., 2004). In the RNA polymerase II transcription, NM1 is necessary for the

formation of the first phosphodiester bond during the initiation phase of transcription (Hofmann et al., 2006). Moreover, NM1 interacts with the B-WICH chromatin remodeling complex and they together participate in the elongation phase of the ribosomal DNA transcription (Percipalle et al., 2006). Additionally, NM1 associates with small ribosomal subunits in the nucleus and it has been shown that it actively participates in their transport from the nucleolus to nuclear pore complexes (Cisterna et al., 2009; Obrdlik et al., 2010). Finally, Chuang and colleagues demonstrated actin-dependent and NM1-dependent directional movement of an activated interphase chromosome site from the nuclear periphery to the nuclear interior (Chuang et al., 2006).

Interestingly, despite the important roles of NM1 in various nuclear events, NM1 knockout (KO) mice prepared in our laboratory were found to be fully viable and fertile (Venit et al., 2013). Moreover, it has been shown that the N-terminal 16 AA extension of NM1 does not serve as a nuclear localization sequence (NLS), as it was originally thought, but instead a unique NLS is present in the second IQ motif of the neck domain shared by all myosin 1c isoforms. Therefore, all myosin 1c isoforms have the ability to enter the cell nucleus (Dzijak et al., 2012). Based on these results it has been proposed that Myo1c participates in nuclear functions attributed to the NM1 protein and fully substitutes for it in case of its absence. Indeed, Venit et al. confirmed this hypothesis and showed that both NM1 and Myo1c are functionally interchangeable in the cell nucleus (Venit et al., 2013). However, phylogenetic evidence suggesting that the NM1 protein was already present in the last common ancestor of vertebrates and tunicates, and the high level of its evolutionary conservation indicate that it might have some important isoform-specific functions (Kahle et al., 2007; Hofmann et al., 2009).

Myosin 1c (Myo1c)

Myosin 1c is the shortest of all myosin 1c isoforms (fig. 1.4). It was discovered in 1992 as the first unconventional myosin in mammals and was initially called mammalian myosin I (Barylko et al., 1992). However, in an effort to unify the nomenclature of class I myosins, it was later renamed to myosin 1c (Myo1c) (Gillespie et al., 2001). Expression analysis revealed a widespread distribution of this protein in different mammalian tissues and immunofluorescence microscopy showed a punctuated membrane localization with a particularly high concentration of the protein at the cell periphery. Specifically, the most

intense staining was in actin-rich leading edges of cells associated with membrane movement, such as filopodia, lamellipodia or growth cones of different cell-types (Wagner et al., 1992). This localization pattern, together with similar observations of protozoan class I myosins, led to a proposal that these molecular motors might participate in motile activity at the cell surface (Pollard et al., 1991; Wagner et al., 1992).

In contrast to NM1, Myo1c has been traditionally considered as exclusively cytoplasmic (Pestic-Dragovich et al., 2000). Therefore, all studies were focused on the role of Myo1c in the cytoplasm, especially in dynamic processes related to the cell membrane. However, it has been shown just recently, that it participates in nuclear processes in a manner similar to NM1 (Venit et al., 2013).

The most well understood is the involvement of Myo1c during mechanical signal transduction in hair cells of the auditory and vestibular systems of the inner ear. Hair cells are mechanoreceptors that posses clusters of 20-300 mechanically sensitive stereocilia protruding perpendicularly from their apical surface membranes (Hudspeth, 2005). These protrusions are structures filled with actin bundles and their membranes contain a small number of large, mechanically gated ion channels, located near the very tips of stereocilia (Ricci et al., 2003). When a mechanical stimulus arrives, such as vibration caused by sound or head movement, the stereocilia are deflected and this bending forces the ion channels to open, causing an inward current of positively charged ions into the hair cell interior which leads to a membrane depolarization and neurotransmitter release (Hudspeth, 2005; Gillespie and Müller, 2009). However, it is necessary that the receptor hair cells remain sensitive even in presence of a continuous stimulation. This is achieved by an adaptation mechanism, which reduces the tension experienced by the ion channels of the deflected stereocilia back to the resting levels, facilitating the re-closing of ion channels, which restores the sensitivity of hair cells to additional stimulation (Holt and Corey 2000; Hudspeth et al., 2000). Myo1c is directly involved in this process as it has been shown that it has an ability to adjust the tension applied on the ion channels by sliding on the stereocilia actin bundles (Holt et al., 2002; Stauffer et al., 2005). The importance of Myo1c in the process of hair cell adaptation has been further confirmed by clinical genetic screening and functional studies, which have linked mutations in the *MYO1C* gene to bilateral hearing loss and other hearing disorders (Zadro et al., 2009; Lin et al., 2011).

Besides its involvement in the process of hearing, Myo1c has an important role in insulin-stimlated glucose uptake in adipocytes and skeletal muscle cells where it is required

for the fusion of GLUT4 glucose transporter vesicles with the cell membrane (Bose et al., 2002; Toyoda et al., 2011). Specifically, it has been shown that Myo1c knockdown and expression of Myo1c actin-binding mutant inhibit the glucose uptake and GLUT4 translocation to the cell membrane and, in contrast, overexpression of wild-type Myo1c increases the level of GLUT4 incorporation (Bose et al., 2002). Myo1c is responsible for the anchoring of GLUT4-containing vesicles to the cortical actin cytoskeleton once the vesicles reach the cell periphery, after being transported along microtubules by kinesin motors (Semiz et al., 2003; Bose et al., 2004). Specifically, GLUT4 vesicles are targeted and anchored to membrane ruffles, which are peripheral regions characteristic by extensive and dynamic actin and cell membrane reorganizations and high local concentrations of Myo1c, which has been implied in their induction (Bose et al., 2004). Furthermore, overexpression of Myo1c in cells where the fusion of GLUT4 vesicles with the cell membrane has been artificially blocked, caused a partial rescue of this block and restored the GLUT4 translocation to the cell membrane. Based on these observations, it has been proposed that Myo1c represents a driving force behind the fusion of GLUT4-containing vesicles with the plasma membrane upon insulin-stimulation, possibly by inducing a localized remodeling of the plasma membrane and without actually binding to GLUT4 vesicles (Bose et al., 2004; Barylko et al., 2005).

Similarly, it has been shown by Arif and colleagues that Myo1c mediates the incorporation of Neph1 and nephrin proteins to plasma membranes of podocytes within the glomeruli in kidney (Arif et al., 2011). It has been shown that Myo1c colocalizes with Neph1 and nephrin proteins in the actin-rich protrusions at the cell periphery. Moreover, this localization of Neph1 and nephrin to the cell periphery is lost by depleting Myo1c (Arif et al., 2011). Additionally, in agreement with its participation in membrane ruffling at leading edges of different cell types, Myo1c knockdown caused an adverse effect on the migration potential of podocytes and on their ability to form a tight, impermeable monolayer (Wagner et al., 1992; Arif et al., 2011). Therefore, Myo1c has an important role in the localization of Neph1 and nephrin proteins to the membrane periphery of podocytes, presumably in a manner analogous to the insulin-dependent membrane localization of GLUT4 transporter in adipocytes (Bose et al., 2004; Arif et al., 2011).

Myo1c is also required in the fertilization-triggered exocytosis of cortical granules and their subsequent compensatory endocytosis and retrieval in the eggs of *Xenopus laevis* (Sokac et al., 2006). It has been shown that following the formation of fusion pores during exocytosis, these vesicles are completely surrounded and compressed by tightly attached actin coats, preventing their collapse and complete fusion with the plasma membrane and

facilitating their retrieval back from the cell membrane (Sokac et al., 2003). Prior to exocytosis, Myo1c proteins are recruited to membranes of cortical granules via their phospholipid-binding tail domain and it has been shown that Myo1c depletion prevents the tight attachment of actin coats to these vesicles, blocks the release of their content and inhibits their retrieval as well (Sokac et al., 2006). Therefore, Myo1c is most likely not involved as a transporter, but as a dynamic linker, tightly coupling the vesicle membrane to the surrounding actin filaments. This tight interaction allows to transform the force generated by actin polymerization into a compression force applied to cortical granules, facilitating the release of their content and their retrieval (Sokac et al., 2006).

Finally, Myo1c has important function in actin and membrane dynamics at the leading edge of cells which has been repeatedly reported as the site of its concentrated localization (Wagner et al., 1992; Bose et al., 2004; Arif et al., 2011; Fan et al., 2012). In podocytes, a wound-healing assay revealed a decrease in the mean rate of migration of Myo1c-depleted cells in comparison to control cells (Arif et al., 2011). Similarly, in epithelial cells, Myo1c has been shown to contribute to actin transport to the cell periphery and cell migration (Fan et al., 2012). Specifically, localized microinjection of purified Myo1c into leading edges of cells caused an increase in localized concentration of monomeric and filamentous actin in this membrane region and induced membrane ruffling and lamellipodia dynamics. In contrast, knockdown of Myo1c reduced the peripheral concentration of actin and the migration potential of endothelial cells (Fan et al., 2012). In B lymphocytes, Myo1c is highly concentrated in actin-rich lamellipodia, filopodia and dendrite-like protrusions generated during cell spreading and it has been shown that generation and maintenance of these structures depends on the presence of functionally intact Myo1c protein (Maravillas-Montero et al., 2011). Furthermore, knockdown of Myo1c in HeLa cells and motile retinal pigment epithelial cells caused a severe reduction in cell spreading, altered the cell morphology and severely reduced migration potential of cells (Brandstaetter et al., 2012).

Interestingly, all Myo1c-related processes described in this section have several common underlying characteristics that are fundamentally related to properties of Myo1c and class I myosins in general (Woolner and Bement, 2009; McConnell and Tyska, 2010; Bond et al., 2013). First, they seem to depend on the ability of Myo1c to interact with both the plasma membrane and the underlying actin cytoskeleton. Second, plasma membrane tension appears to be a major regulator of these processes (Diz-Muñoz et al., 2012). It has been suggested that class I myosins, including Myo1c, alter their kinetic and biomechanical properties in response

to changes in the applied mechanical tension and can act as molecular force sensors (Laakso et al., 2008). Indeed, these proteins apparently serve as dynamic linkers mediating the interaction between cell membrane and the underlying cortical actin network (fig. 1.5) and thus contribute to the maintenance of membrane tension (Nambiar et al., 2009). This further supports a regulatory role of Myo1c in the aforementioned membrane-related processes.

Isoform A

Recently, a third *MYO1C* gene product called isoform A (Myo1c-isoA) has been identified. Similarly to NM1, Myo1c-isoA differs from the Myo1c isoform by an N-terminal extension of 36 AA, 10 of which are shared with NM1 and the remaining 26 AA come from the Myo1c-isoA-specific exon -2 (fig. 1.4) (Ihnatovych et al., 2012). Unlike NM1, which is ubiquitously expressed at comparable levels in various mouse tissues, Myo1c-isoA shows a tissue-specific expression pattern and its presence has been detected only in kidney, adrenal gland and in a subset of adipose tissues. However, even in these tissues, the Myo1c-isoA expression levels are extremely low in comparison to expression levels of NM1 (Sielski et al., 2014) and a little is known about the functional significance of the Myo1c-isoA. However, the tissue-specific expression pattern and different regulation of Myo1c-isoA expression indicate that it may have some tissue-specific and isoform-specific functions (Sielski et al., 2014). Indeed, it has been shown that Myo1c-isoA interacts with RNA polymerase II and, similarly to NM1 and Myo1c, this interaction is lost upon transcription inhibition, but it has not been found in nucleoli and no interaction with RNA polymerase I has been detected (Ihnatovych et al., 2012). Therefore, it is possible that Myo1c-isoA has individual functions that do not overlap with functional roles of NM1 and Myo1c.

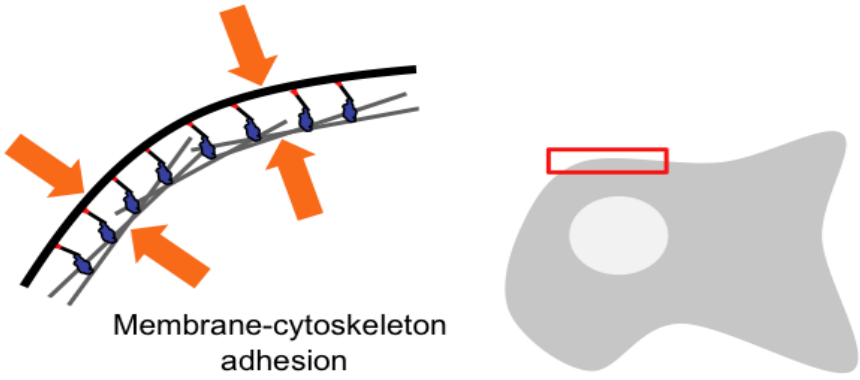

Figure 1.5. Several class I myosins, including Myo1c, have been shown to act as linkers in the membrane-cytoskeleton adhesion and participate in the maintenance of plasma membrane tension. *Figure was taken and adapted from McConnell and Tyska, 2010.*

2. Atomic force microscopy

A unifying property of all living biological systems and their components – including single molecules, molecular complexes and cells – is their inherent dynamic nature and heterogeneity. These characteristics allow them to perform various physiological functions at all levels of a living organism, including metabolism, proliferation and response to various external stimuli. However, the dynamic property of many biological samples also poses significant technical challenges for their study and understanding. The trade-off between techniques such as electron microscopy that performs high-resolution imaging but requires sample fixation and lower-resolution live-cell fluorescent imaging serves as a good example of one such technical challenge. With that regard, over the last two decades, atomic force microscopy (AFM) (Binnig et al. 1986) has emerged as a high-resolution tool that offers a unique opportunity to study the dynamic properties of living biological systems under near-physiological conditions. Specifically, it offers a combination of nanometer-scale imaging of a three-dimensional (3D) sample topography and complementary measurements of various biophysical properties such as elasticity, stiffness or adhesion (Dufrêne et al. 2013).

2.1 Basic principle of atomic force microscopy

AFM is a member of a diverse group of microscopic techniques called scanning probe microscopies which are based on raster scanning of the sample surface using a tip of a small probe (Santos and Castanho, 2004). During the process of scanning, the tip of the probe is brought into contact with the sample surface and changes in various tip-sample interactions are recorded. Specifically, atomic force microscope detects and records changes in local attractive and repulsive interaction forces that occur between atoms at the tip of the AFM probe and atoms of the sample surface during the process of scanning, including Van der Waals, electrostatic and hydration forces (Butt, 1991). The obtained force data can then be used for the reconstruction of the sample 3D surface topology as well as for characterizing its mechanical properties (Santos and Castanho, 2004; Dufrêne et al. 2013).

The most fundamental component of any AFM system is a small probe attached to a extremely flexible cantilever spring (fig. 2.1). The probe often has a conical shape, its tip is of

varying sharpness with tip radius less than 50 nm and the length of the cantilever is typically around 100 μm (Kaemmer, 2011). The probe and the cantilever are commonly both manufactured as a single piece made from silicon or silicon nitride (Si_3N_4) (Zhong et al., 1993; Kaemmer, 2011). While the tip of an AFM probe is brought into contact with the sample during raster scanning of the sample surface, it is affected by attractive and repulsive tip-sample interaction forces which leads to a deflection of the cantilever in the vertical direction (Butt, 1991). Depending on the specific mode of operation, the tip can be either in a continuous contact with the sample or it may contact the sample periodically in an up-and-down vertical periodic movement.

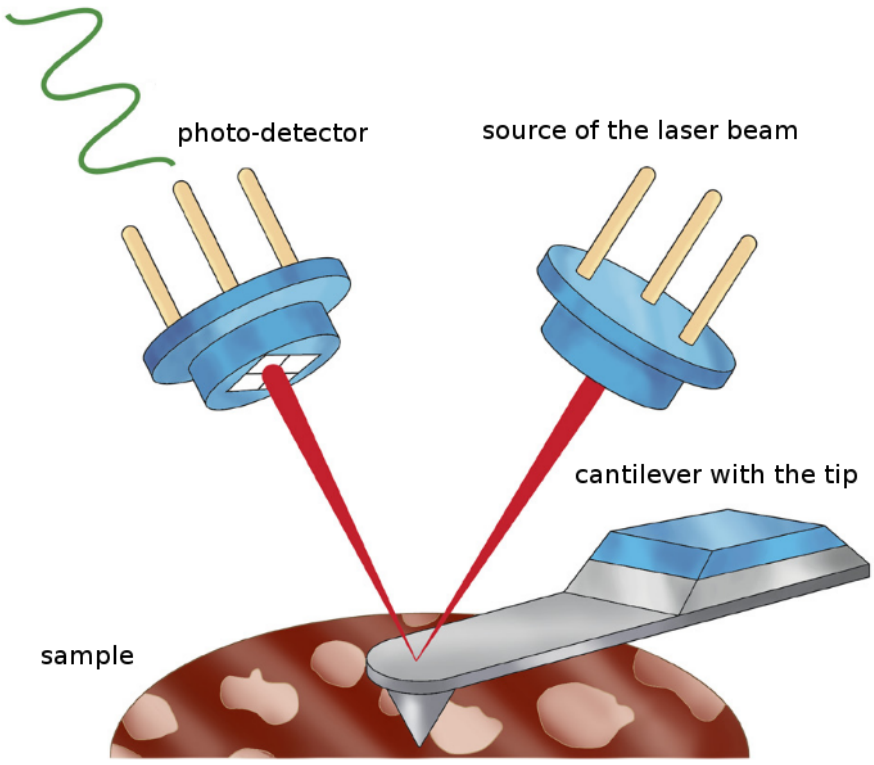

Figure 2.1. Basic componensts of an atomic force microscope. *Figure was taken and adapted from Kaemmer, 2011.*

Therefore, AFM does not actually measure the interaction forces between the tip and the sample directly. Instead, it measures the amount of deflection of the cantilever by monitoring the movement of a laser beam focused on the tip-carrying end of the cantilever and reflected into a position-sensitive photo-detector (fig. 2.1) (Meyer and Amer, 1988). The changes of the

cantilever deflection are then converted to values of interaction forces that caused this deflection. Specifically, if the AFM probe is indented into the sample causing a cantilever bending by d, then, according to Hooke's law, a force F required to bend a spring (in this case, a cantilever) by a distance d (cantilever deflection) is directly proportional to that distance (Domke and Radmacher, 1998). That is,

$$F = k \cdot d$$

where k is the known spring constant (a parameter representing the stiffness of the used cantilever that depends on its shape and material) (Domke and Radmacher, 1998). Therefore, it is possible to calculate the amount of the tip-sample interaction force for a given value of cantilever deflection at any moment during the process of scanning. Moreover, because of the extreme sensitivity of the optical detection mechanism of cantilever deflection, AFM is able to detect interaction forces with a piconewton sensitivity (Dufrêne et al. 2013).

2.2 Modes of AFM operation

Contact mode

Since the invention of AFM, contact mode has been the default mode of AFM operation (Binnig et al. 1986). During contact mode, an AFM probe is first brought into close proximity with the sample. Then, the sample surface is scanned in parallel lines by moving the probe over the scan area while maintaining the deflection of the cantilever approximately constant. Specifically, whenever the tip of the probe encounters an upward or downhill tilt on the sample surface, the AFM records the change in the cantilever deflection caused by the change in the tip-sample interaction forces and the vertical position of the probe is readjusted accordingly. This is achieved through the feedback mechanism which modifies the vertical position of the probe based on real-time values coming from the deflection detector. Values of cantilever deflection recorded for each point in the scan area then allow a reconstruction of the 3D topography of the sample surface (Santos and Castanho, 2004).

Despite its simplicity, contact mode AFM has several disadvantages. First, dragging lateral forces exerted on the sample by the tip can cause shearing of the sample, which can be

especially problematic when one measures living cells. Second, the tip of the AFM probe itself can break off if it encounters a particularly hard spot on the sample surface (Zhong et al., 1993).

Tapping mode

Tapping mode of the AFM has been developed as an improvement of the original contact mode. Instead of keeping the tip of the probe and the sample constantly in close proximity as in contact mode, in tapping mode, the cantilever is oscillated near its resonance frequency (approximately 300kHz) in a vertical direction, perpendicularly to the sample surface (Zhong et al., 1993). In each period of the oscillation, the tip of the AFM probe contacts the surface of the sample and indents into it for only a brief moment which eliminates the damaging shearing effect of lateral forces (Zhong et al., 1993). In tapping mode, a feedback system detects disturbances in the cantilever amplitude oscillation caused by tip-sample interaction forces during each contact. Based on these these disturbances, it immediately modifies the vertical position of the cantilever above the sample accordingly to maintain the oscillation amplitude constant (Zhong et al., 1993). Since the changes of the vertical cantilever positions are recorded for each point of contact in the scanning area, tapping mode AFM allows a reconstruction of the 3D topography of the sample, similarly to AFM in the contact mode. Furthermore, the changes in the tip-sample interaction forces during each single contact are recorded in the form of force curves, which allow extraction of various physical properties of the sample, as will be discussed bellow.

PeakForce tapping mode

Recently, a further improvement of the tapping mode AFM, called PeakForce tapping (PFT) mode, has been implemented (Pittenger et al., 2011). In principle, PFT mode is quite similar to the conventional tapping mode. The AFM probe is moved over the sample in a raster-like fashion while it is periodically moved in a vertical direction, measuring the changes in the tip-sample interaction forces at discreet locations on the sample surface. However, unlike in tapping mode, the cantilever in PFT mode oscillates at frequencies far bellow its resonance frequency, typically 1-2 kHz (Berquand, 2012). Moreover, the feedback system directly monitors the amount of tip-sample interaction forces in real-time. Specifically, it maintains the maximum values of interaction forces at an approximately constant level by forcing the

cantilever to move upwards whenever the interaction forces reach a defined threshold value. This limits the amount of force exerted by the tip on the sample during each contact and narrows the possibility of causing a potential damage to the sample or the probe itself (Pittenger et al., 2011). This is in contrast to the traditional tapping mode AFM where the amplitude of cantilever oscillation is kept constant regardless the level of the interaction force at any point of the approach-retract cycle.

2.3 Approach-retract cycle of the PeakForce tapping mode

Although being very suitable for high-resolution imaging of a wide range of different samples, AFM is more than just an alternative microscopic technique. Specifically, in the so-called force-volume imaging mode (Dufrêne et al., 2013), the AFM performs a raster scan of a given area of the sample surface at a specified resolution and records a two-dimensional (2D) array of force measurements. Analysis of these measurements can then provide information about the spatial distribution of various physical properties, such as sample elasticity or adhesion. A model example of a force measurement performed during one period of the approach-retract cycle of the PFT mode AFM, describing changes in the interaction force as a function of time, is shown in fig 2.2a.

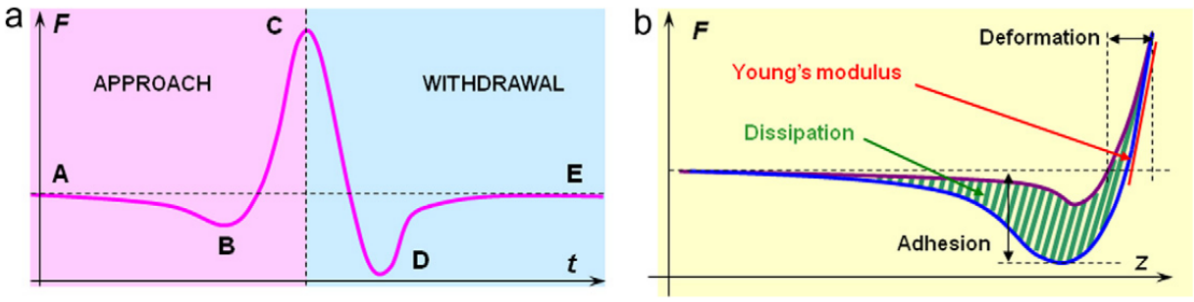

Figure 2.2. AFM force curves. ***(a)*** *Force curve showing changes in tip-sample interaction forces during a single period of the approach-retract cycle of the PeakForce Tapping mode AFM at a given point on the sample surface. The curve describes the change of interaction forces as a function of time.* ***(b)*** *A pair of force-versus-indentation curves calculated from the raw force recordings shown in (a), split at the peak force point C. From the force-versus-indentation curves, various sample properties can be extracted, including the amount of sample deformation, adhesion force, energy dissipation or Young's modulus of elasticity. Figure was was taken and adapted from Heu et al., 2012.*

At the beginning, the probe is far above the surface and no interaction between the tip and the surface is detectable (fig 2.2a, point A). As the tip moves closer to the surface, it experiences attractive forces, especially Van der Waals interaction, between the sample and the tip, that pull it closer to the sample surface (this corresponds to an observed slightly negative interaction force) (fig 2.2a, point B). When the cantilever pushes the tip further into the sample, there is a rapid rise in repulsive force, namely electrostatic and hydration forces, caused by the cantilever pushing the atoms of the tip and the atoms of the sample close together. The indentation of the probe into the sample continues until the the repulsive force reaches its peak value (fig 2.2a, point C), which is a threshold that triggers the feedback system to withdraw the tip from the sample. The cantilever is then forced to withdraw, which is accompanied by a rapid decrease of repulsive forces. Finally, before the tip and the sample are separated, attractive forces keep the tip of the probe and the sample surface together for a short time until this adhesion breaks (fig 2.2, point D). The cantilever is then positioned above the surface and the interaction forces become zero again (fig 2.2, point E). At this point, the probe is moved laterally and is ready for next period of the approach-retract cycle at a neighboring location on the sample surface (Berquand, 2012).

2.4 Force-versus-indentation curves

The peak force value at the point C in fig. 2.2a represents a threshold which triggers the feedback system to withdraw the cantilever out of the sample. This peak force point can be used to split the force data in two parts, one for the approach phase and one for the retract phase (fig. 2.2a, purple and blue). Moreover, since the PFT mode AFM directly controls the height of the cantilever above the surface at each point in time, it is possible to plot the interaction force changes during approach and retract phases as functions of the vertical position of the cantilever instead of functions of time. However, to be able to extract information about sample mechanical properties, these force curves have to be converted into pairs of the so-called force-versus-indentation curves (fig. 2.2b, purple and blue), which describe the changes in tip-sample interaction forces as functions of the indentation depth of the tip into the sample (Pittenger et al., 2011; Lekka et al., 2012b).

From these force-indentation curves a number of various sample properties can be obtained (fig. 2.2b) (Pittenger et al., 2011). For example, the value of adhesion force between the tip and the sample can be calculated as a vertical distance between the zero baseline force

and the most negative force of the retract curve. The distance between the contact point and and the depth of the maximum indentation caused by the peak force trigger value gives the amount of sample deformation. Furthermore, the area between an approach curve and a retract curve represents the amount of energy dissipation (Heu et al., 2012). However, in biophysical studies of cell surface properties, the most frequently used parameter is the Young's modulus (YM).

YM can be computed by fitting a line through the steep portion of the retract curve (fig. 2.2b) and represents a measure of elasticity of the material corresponding to a ratio between an amount of stress applied to a material and a strain caused by this tension (Heu et al., 2012). Specifically, while lower values of YM correspond to higher elasticity of the sample, higher YM values indicate its higher stiffness and rigidity (Heu et al., 2012). Importantly, YM is only a relative value and cannot be used as an absolute comparative measure of elasticity of biological samples, since it is extremely sensitive to changes in various external experimental conditions as well as changes in parameters of the AFM system itself (Lekka et al., 2012b). Indeed, previous AFM measurements of eukaryotic cells performed using different probes, cantilevers, scanning speeds, different cell substrates and other experimental variables revealed an extremely wide range of possible YM values (Kuznetsova et al., 2007; Lekka et al., 2012b). Therefore, to be able to perform comparative studies of sample elasticity using absolute values of YM, all experimental conditions must be preserved (Lekka et al., 2012b).

3. Motivation and background

The importance of Myo1c in cytoplasmic processes has been already well established. Specifically, it participates in a number of different plasma membrane-related events, such as regulation of mechanosensitive ion channels, exocytosis, endocytosis, cell motility or cell spreading (Barylko et al., 2005; McConnell and Tyska, 2010; Bond et al., 2013). Moreover, based on kinetic and biomechanical properties of class I myosins, it has been proposed that these proteins, including Myo1c, have a regulatory role in these events, acting as dynamic linkers between the cell membrane and the underlying actin cytoskeleton (fig. 1.5), and have the ability to sense and respond to changes in mechanical tension (Laakso et al., 2008; Nambiar et al., 2009). A significant evidence has been gathered supporting the involvement of NM1 in important nuclear functions (Pestic-Dragovich et al., 2000; Philimonenko et al., 2004; Hofmann et al., 2006; Percipalle et al., 2006; Cisterna et al., 2009; Obrdlik et al., 2010). However, interestingly, NM1 knockout (KO) mice prepared in our laboratory are fully viable and fertile without any obvious defective phenotype related to its nuclear functions and it has been shown that the Myo1c isoform participates in these nuclear functions as well (Venit et al., 2013). In fact, although being traditionally regarded as exclusively cytoplasmic or nuclear, it has been shown that all myosin 1c isoforms have the ability to enter the cell nucleus and they are all present in the cytoplasm as well (Dzijak et al., 2012). Moreover, analysis of nuclear and cytoplasmic fractions by western blotting indicates that 60% of the total cellular pool of NM1/Myo1c resides in the cytoplasm and 40% is localized in the cell nucleus. Furthermore, the ratio of NM1 and Myo1c in both compartments is approximately equal (Kalendová, unpublished data).

While investigating the potential phenotypic differences between wild-type (WT) and NM1 KO mice, we have noticed a rather interesting phenomenon. When we exposed skin fibroblasts derived from both strains of mice to hypotonic stress conditions, we have discovered that the NM1 KO cells have significantly higher survival rates in comparison to WT cells. Moreover, the survival of WT cells overexpressing exogenous NM1 from a lentivirus expression vector drops even lower, while the survival rate of NM1 KO cells with overexpression of NM1 is shifted back towards the WT phenotype. Additionally, comparison of microarray expression profiling of both cell lines revealed a change in expression of genes functionally related to the cell membrane and cytoplasm in NM1 KO (Venit and Kalendová,

manuscript). These observations lead us to a hypothesis that, although studied exclusively for its presence in the cell nucleus, NM1 is involved in cytoplasmic processes, particularly in those related to the maintenance of cell membrane tension. Specifically, given the actin-binding and PIP_2-binding properties of all Myo1c isoforms (Hokanson et al., 2006b), we propose that NM1 serves as a linker between the cell membrane and cortical actin cytoskeleton, possibly controlling the cell membrane tension, similarly to other class I myosins (Nambiar et al., 2009).

Based on these assumptions, we hypothesised that the survival rate of NM1 KO fibroblasts under hypotonic stress is higher because their plasma membrane is more flexible to stretching since they completely lack the NM1 protein, one of the linkers between the cell membrane and actin cytoskeleton (fig. 3.1). Therefore, when exposed to a strong hypotonic environment, the more flexible membrane allows NM1 KO cells to absorb more water that is being forced inwards by osmotic forces. In contrast, the cell membranes of WT fibroblasts are more rigid, less flexible and more tightly attached to the underlying cortical actin cytoskeleton. This makes the WT cells more susceptible to hypotonic lysis, since their rigid membrane is not able to stretch as much as in the case of NM1 KO cells.

Therefore, the main purpose of this study was to test our hypothesis and investigate, whether the NM1 protein participates in plasma membrane-related events, in a manner similar to other class I myosins, and if it contributes to the maintenance of plasma membrane tension.

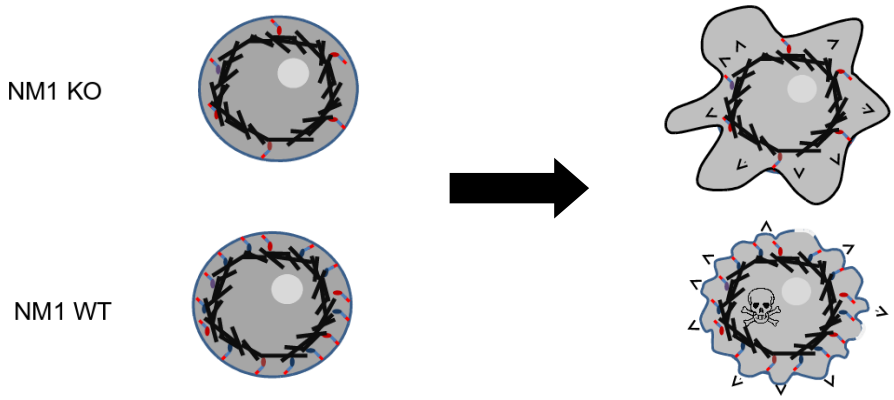

Figure 3.1. Hypotonic stress response of mouse WT and NM1 KO fibroblasts – a hypothesis. *Due to the absence of NM1 protein, plasma membrane of NM1 KO cells is more loosely attached to the underlying cortical action. This makes the membrane more flexible, allowing the cell to absorb more distiled water from the hypotonic environment. In contrast, plasma membranes of WT cells have a higher tension and are more tightly attached to the cortical actin network. Therefore, WT cells are more susceptible to the hypotonic lysis, since their rigid membrane does not allow them to swell as much as in case of NM1 KO cells. Taken and adapted from Venit and Kalendová, manuscript.*

4. Aims

The main focus of this study was to find out, whether nuclear myosin 1 (NM1) participates in membrane-related events and if it contributes to the maintenance of plasma membrane tension. Specifically, our aims have been following:

1. Characterize the localization pattern of NM1 at the plasma membrane using fluorescence microscopy and compare it to the cellular distribution of the myosin 1c isoform (Myo1c).

2. Determine whether the localization of NM1 to the cell periphery depends on actin filaments, or its phospholipid-binding ability.

3. Characterize the elastic properties of mouse WT and NM1 KO skin fibroblasts using atomic force microscopy (AFM). Investigate whether NM1 protein participates in the maintenance of plasma membrane tension in skin fibroblasts and compare the membrane elasticity of these cells to some human cell-line.

4. Describe the possible phenotype of NMI KO cells. Compare the heights of WT and NM1 KO fibroblasts using AFM scan data of the cell surface. Compare the actin distribution in mouse WT and NM1 KO skin fibroblasts using fluorescence microscopy and check whether the loss of NM1 leads to alterations in the distribution of actin filaments or cell spreading.

5. Materials and methods

Cell lines

Mouse WT and NM1 KO stable skin fibroblast cell-lines

Primary cultures of skin fibroblasts were derived from ear tissue of WT and NM1 KO mice prepared earlier in our laboratory (Venit et al., 2013). Explanted tissue samples were washed with PBS and incubated for 60 min in 0.3% trypsin/PBS (Sigma-Aldrich) at 37°C in a water bath. Explants were then dissected into small pieces using scalpel, put into Petri dish, weighted down by sterile glass coverslips and supplied by complete cell culture medium. The medium was changed regularly every third day until the primary culture cells, migrated out of the explanted tissue, grew to confluence, after which they were passaged. In our experiments, we used stable skin fibroblasts which were prepared by long-running cultivation of over twenty repeated passages. Cells were incubated at 37 °C in a humidified atmosphere containing 5% CO_2 in full D-MEM cell culture medium. For our rescue experiments, we used NM1 KO fibroblasts stably expressing exogenous NM1 protein from a lentiviral expression vector prepared in our laboratory as described previously (Venit et al., 2013).

Human osteosarcoma U2OS cell-lines

For the purposes of this work, we used human osteosarcoma U2OS cell-lines (American Type Culture Collection No. HTB-96) expressing WT and mutant NM1 isoforms, kindly provided by Alžběta Kalendová and prepared using lentiviral transduction. Briefly, U2OS cells were transduced with lentivirus carrying shRNA targeting only human *MYO1C* gene products and a control cell-line was transduced with a lentiviral vector expressing non-targeting shRNA. U2OS human-*MYO1C* knockdown cells were then transduced with a second lentivirus carrying shRNA-resistant mouse WT NM1 protein, mouse RK605AA NM1 mutant (unable to bind actin) and mouse K908A NM1 mutant (unable to bind PIP_2), respectively (Venit and Kalendová et al., manuscript). All U2OS cells were incubated in full D-MEM cell culture medium at 37 °C in a humidified atmosphere containing 5% CO_2.

Cell culture medium

All cells were cultivated in complete growth Dulbecco's modified Eagle's medium (D-MEM, Sigma-Aldrich) with an addition of 10% fetal bovine serum (Invitrogen), 50 U/ml penicillin (Sigma-Aldrich) and 50 μl/ml streptomycin (Sigma-Aldrich).

Cell passaging

The culture medium was aspirated from the Petri dish and cells were carefully washed two times with room-temperature 1× PBS (Sigma-Aldrich). Cells were then incubated at 37 °C in an appropriate amount of trypsin (Sigma-Aldrich) until they completely dissociated from the substrate, which was checked under an inverted microscope (approximately 10 min). An appropriate volume of medium was then added to each Petri dish to inactivate trypsin solution, clumps of cells in suspension were dissolved by pipetting and cells were split equally to a desired number to new Petri dishes for further cultivation.

Antibodies

For immunodetection of myo1c isoforms in human U2OS cells (NM1, Myo1c, isoA) and mouse skin fibroblasts (NM1 and Myo1c), rabbit polyclonal anti-MYO1C primary antibody (Sigma-Aldrich, cat. no. HPA001768, 100× dilution) was used in combination with donkey anti-rabbit IgG secondary antibody (Jackson, cat. no. 711-175-152, 100× dilution) for staining in human cells and goat anti-rabbit IgG secondary antibody (Invitrogen, cat. no. A21429, 400× dilution) for staining in mouse fibroblasts. For immunofluorescence analysis of actin distribution and cell spreading in mouse skin fibroblasts, mouse monoclonal anti-β-actin primary antibody (Sigma-Aldrich, cat. no. A5316, 1000× dilution) was used together with goat anti-mouse IgG secondary antibody (Invitrogen, cat. no. A21424, 400× dilution).

Immunofluorescence

Cells were grown on on glass coverslips to a desired concentration overnight at 37 °C in full D-MEM cell culture medium in a humidified 5% CO_2 atmosphere. Next day, the medium was aspirated, cells were washed twice by 1× PBS, and after 20 min fixation in 4%

paraformaldehyde (Sigma-Aldrich) in PBS at room temperature, they were permeabilized for 10 min in 0.1% Triton X-100 (Polysciences Inc.) in PBS. After three washes with PBS-T (0.05% Tween 20 from Polysciences Inc. in PBS), coverslips were incubated in a wet chamber for one hour with 20 µl of a primary antibody (properly diluted in PBS-T) per coverslip. After additional three washes with PBS-T, coverslips were incubated with 20 µl of a properly diluted secondary antibody. Finally, after three washes with PBS-T, coverslips were mounted on microscopic slides using ProLong Gold antifade reagent with DAPI (Invitrogen). Fluorescence images were acquired using Leica DM6000 B inverted microscope with 60X/100X immersion oil objective lens and exported using LAS AF software (Leica, version 2.6.0.7266). The final processing of exported images was done using an open-source GIMP image editor (version 2.8.6).

Atomic force microscopy

All measurements of cell membrane properties of mouse skin fibroblasts were performed on the BioScope Catalyst™ atomic force microscope (Bruker) mounted on the stage of Leica DMI 6000 inverted microscope (Leica). The experiments were done in a laboratory of the Bruker company in Karlsruhe, Germany, which kindly allowed us to use their equipment and provided us with their valuable expertise. Experiments on human U2OS cells were performed using the same type of AFM mounted on the Olympus IX81 inverted microscope (Olympus) at the Institute of Molecular and Translational Medicine of the Faculty of Medicine and Dentistry of Palacký University in Olomouc, Czech Republic. In both cases, silicon nitride DNP-10 probes (Bruker) were mounted on the type B cantilever (Bruker) and the AFM was operated and controlled by a proprietary Broker control software in the PeakForce Tapping mode (Kaemmer, 2011; Pittenger et al., 2011).

A day before the measurement, cells were grown overnight on 50mm glass bottom Petri dishes (WillCo Wells BV) in a full D-MEM cell culture medium at 37 °C in a humidified atmosphere containing 5% CO_2. Next day, plasma membrane elasticity measurements were performed on living cells in glass bottom Petri dish with fresh full D-MEM cell culture medium, and since both microscopes had heated stages, a constant temperature of 37 °C was maintained during the measurements. The AFM experiments themselves were realized as follows. First, each cell was localized using an inverted optical microscope, a cantilever carrying an AFM probe was brought over the cell into a close

proximity of its surface and the scanning process was engaged. The scan surface area was a 30–40 μm square and for each cell, an array of 64×64 (i.e. 4096) individual force curves were recordered and saved as Peak Force Capture raw scan data file.

The following parameters of the AFM system were established during the calibration prior to the measurements. In case of mouse fibroblasts: scan rate 0.3 Hz, cantilever deflection sensitivity 35 nm/V, cantilever spring constant 0.197 N/m, tip radius 20 nm, tip half-angle 18º, Poisson's ratio 0.4. In case of human U2OS cells: scan rate 0.331 Hz, cantilever deflection sensitivity 28.5 nm/V, cantilever spring constant 0.08 N/m, tip radius 20 nm, tip half-angle 18º, Poisson's ratio 0.4. In total, ten WT, ten NM1 KO, seven rescued NM1 KO mouse skin fibroblasts and five U2OS control and five U2OS *MYO1C*-knockdown U2OS cells were measured and their properties were analyzed as described bellow.

Computing the Young's modulus of elasticity

The mechanical properties of cell membranes were expressed using Young's modulus (YM, in pascal units), which is a physical quantity representing a sample elasticity and corresponds to a ratio between an amount of stress applied to a sample and a strain induced by this stress (Heu et al., 2012). Specifically, while lower values of YM correspond to a higher elasticity of the sample, higher YM values indicate its higher stiffness and rigidity (Heu et al., 2012).

The analysis of membrane elasticity was performed using a proprietary Bruker NanoScope Analysis application (Bruker, version 1.40) and an open-source R programming environment (version 3.0.1) with *xlsx*, *ggplot2* and *lattice* package extensions available from the CRAN package repository. First, for each measured cell, a corresponding Peak Force Capture scan data file was loaded into the NanoScope Analysis application. Using the Force Volume tool of the software, a region of interest on the cell surface above the nucleus (fig. 6.5B) or closer to the cell periphery (fig. 6.8) was selected on an image height map. Then, a set of force curves for each pixel in the selected cell surface area was exported as individual files.

The calculations of the YM of elasticity were performed for each force curve file from a given cell individually. First, a randomly chosen force curve was loaded into the NanoScope Analysis software and the values of deflection sensitivity, spring constant, tip radius, tip half-angle and Poisson's ratio parameters were set accordingly as specified above using the Modify Force Parameters tool. The YM value from the force curve itself was then calculated

using an Indentation tool by fitting a Sneddon's model of the tip-sample interaction (Sneddon, 1965) to the linear portion of the retract force-indentation curve as described previously (Heu et al., 2012). Additionally, the fit region was restricted by setting the Max/Min Force Fit Boundaries to 60%–10% of the vertical force axis, since the Sneddon's model described the retract force-indentation curve most accurately in this force range. Finally, after the YM value for a single curve was calculated, the same method was applied to all remaining force curve files in a batch-processing mode using the Run History tool, and all values of YM for each individual force curve obtained from a given cell were then exported in a Microsoft Excel spreadsheet format. The described process was performed for all scanned cells.

The final processing and analysis of YM datasets were performed using the R programming environment and its statistical and plotting functionality. Importantly, since the number of force curves gathered from each cell was not always equal, only a random subset of 350 values of calculated YM from each cell was included in the analysis, to avoid a potential bias from cells where a number of recorded force curves was significantly larger.

Visualization of spatial distribution of membrane elasticity

The image maps showing the spatial distribution of membrane elasticity were calculated for each cell of interest from the corresponding YM dataset exported from the NanoScope Analysis AFM software. First, a square region of the cell membrane above the nucleus was selected on the image height map, such that the number of curves in that selected region was equal to a square root of N for some integer N (18-20), and a set of $N \times N$ YM values was calculated from the corresponding force curves as described in the previous section. The construction of the visual elasticity maps were performed using our custom made R script as follows.

First, YM fit data stored the Excel spreadsheet were loaded into R using the *read.xlsx* function from the *xlsx* extension package (the `'>'` character represents a command-line prompt of the R programming language):

```
> ym_data <- read.xlsx([filename], header = FALSE, 1, startRow = 9)
> ym_data <- head(ym_data, -4)
> ym_data <- ym_data[ , 1:4]
```

Then, since the YM values in the Excel table were not stored in the order in which they were captured, they were sorted to the linear order by following commands:

```
> ym_data$X1 <- as.numeric(gsub("^.*-.*-", "", ym_data$X1))
> ym_data <- ym_data[order(ym_data$X1), ]
```

All YM values were then converted from a linear vector into a two-dimensional matrix and this matrix was rotated clockwise by 90° to rearrange the reconstructed YM matrix into a proper orientation:

```
> rotate <- function(mat) t(apply(mat, 2, rev))
>
> N <- sqrt(nrow(x))
> ym.matrix <- rotate(matrix(ym_data$X3, nrow = N, ncol = N))
```

Finally, YM values in the constructed matrix were assigned a color from a specified color gradient and plotted as a color heatmap using the *levelplot* command from the *lattice* R extension:

```
> levels <- 50
> colors <- colorRampPalette(c("green", "red", "blue"))(levels)
> print(levelplot(ym.matrix, xlab = "", ylab = "", at = seq(0.1, 2.5,
>              length.out = levels - 1), scale = list(y = list(at=c()),
>              x = list(at = c())), col.regions = c(colors)))
```

Analysis of cell heights

For each measured cell, a corresponding Peak Force Capture raw scan data was loaded into the NanoScope Analysis application. Using the Section tool, a cross-section was performed over the reconstructed cell height map going through the highest region of the cell surface as shown in fig. 6.12A. The cell profile curve, representing a relative change of the cell height along the section line, was then exported from NanoScope Analysis to a text file containing two columns of numbers describing the position on the section line and the corresponding relative height (fig. 6.12B). These data were then analyzed using the R programming language as follows.

For each cell, a text file containing the cell profile data was loaded into R. Then, the relative height at each given point of the section line was normalized to a zero baseline, corresponding to the zero height level of the substrate, to obtain a vector containing the true values of the cell height:

```
> cell_section <- read.table([filename], header = TRUE, sep = "\t")
> cell_section[ , 2] <- cell_section[ , 2] - min(cell_section[ , 2])
```

After this correction, the true maximum of the cell height could be calculated and the whole cell height profile could be plotted as follows:

```
> max_cell_height <- max(cell_section[ , 2])
>
> len <- cell_section[ , 1]
> height <- cell_section[ , 2]
> plot(len, height, ylim = c(0, 4), type = "l", ylab = "height [um]"),
>      xlab = "length along the section line [um]")
> points(len[which.max(height)], height[which.max(height)],
>        col="red", pch=20)
> legend("topleft", paste("max =", max(height), "um"), col="red",
>        pch=20)
```

Statistics

The tests of statistical significance were carried out using an unpaired two-sample Student's t-test implemented as a built-in *t.test* function of the R programming environment. The levels of statistical significance were 0.05 or 0.01 and are always explicitly noted. Values in the text are shown as mean ± S.D. The plots of final AFM data are shown as density plots and boxplots. Density plots describe a continuous distribution pattern of a set of values over a specific range, similarly to histograms. A height of the boxplot represents an interquartile range, line horizontally crossing the boxplot represents a median value and the upper and bottom whiskers extend to lowest and highest detected extreme values. For the plotting purposes, the built-in plotting functionality of the R programming environment and its *ggplot2* extension package were used.

6. Results

Myosin 1c isoforms localize to the plasma membrane and cell periphery

Early studies of class I myosins in different cell types have shown a predominant localization of these motors to the plasma membrane and their particular enrichment at the cell periphery, in regions associated with motile activity (Wagner et al., 1992). In further research, we used human osteosarcoma U2OS cells and mouse skin fibroblasts to determine whether myosin 1c isoforms share a similar localization pattern as was previously described in other cell-lines. To do that, we used antibody targeting the tail domain shared by all myosin 1c isoforms (Myo1c and NM1 in mice, Myo1c, NM1 and Myo1c-isoA in humans).

We have found that the distribution pattern of myosin 1c isoforms in U2OS human cell-line closely resembles those reported in previous studies of different cell-types (Wagner et al., 1992; Bose et al., 2004; Arif et al., 2011). Specifically, myosin 1c isoforms show a punctuated distribution on the plasma membrane with a particularly high concentration in various cell membrane protrusions at the cell periphery (fig. 6.1A). This was further proved by immunofluorescence staining of U2OS cells with all myosin 1c isoforms depleted by RNA interference, in which the fluorescence signal on the plasma membrane was significantly decreased. However, the localization pattern of myosin 1c isoforms at the plasma membrane and in membrane protrusions remained the same, albeit significantly less pronounced due to the lower amount of MYO1C protein products (fig. 6.1B).

Immunolocalization of myosin 1c isoforms in WT mouse skin fibroblasts revealed a slightly different localization pattern. While we have still observed a dotted distribution pattern over the whole surface of the plasma membrane, in contrast to U2OS cells, which often showed a high concentration of myosin 1c isoforms along the cell border and in membrane protrusions, we have observed only discreet and highly localized peripheral patches of the fluorescence signal (fig. 6.2A). Moreover, immunofluorescence staining of NM1 KO fibroblasts revealed an overall reduction of the plasma membrane fluorescence signal and, in particular, loss of the localized fluorescence patches at the cell periphery, suggesting that NM1 is indeed present at the plasma membrane of WT fibroblasts (fig. 6.2B).

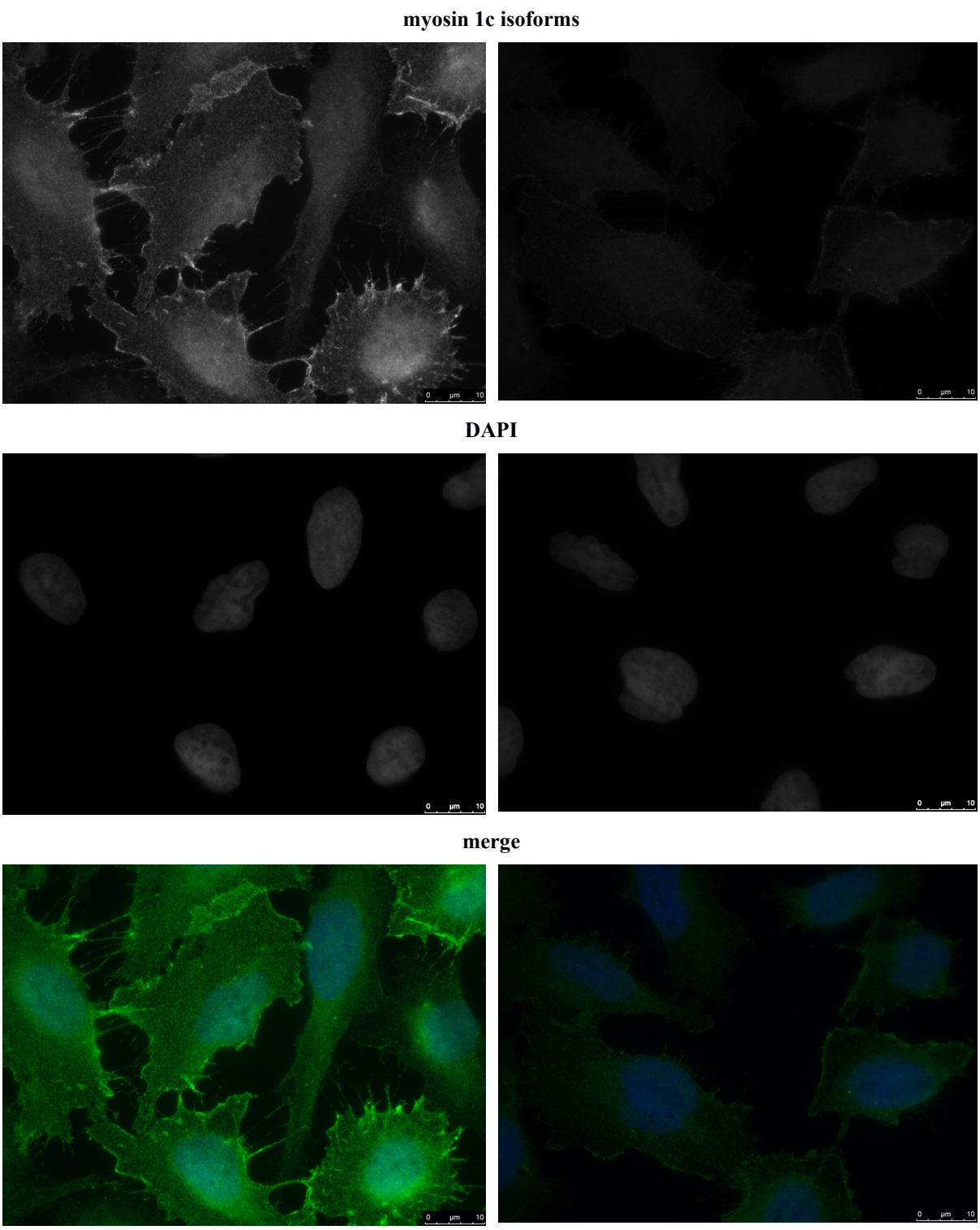

Figure 6.1. Cellular localization pattern of myosin 1c isoforms in the U2OS human cell-line. (A) *Control U2OS cells show a punctuated distribution of myosin 1c isoforms on the plasma membrane with a particularly high concentration at the cell periphery and in various cell membrane protrusions.* ***(B)*** *Knockdown of all myosin 1c isoforms caused a significant reduction in the fluorescence signal. However, the localization pattern remains similar as in control cells.*

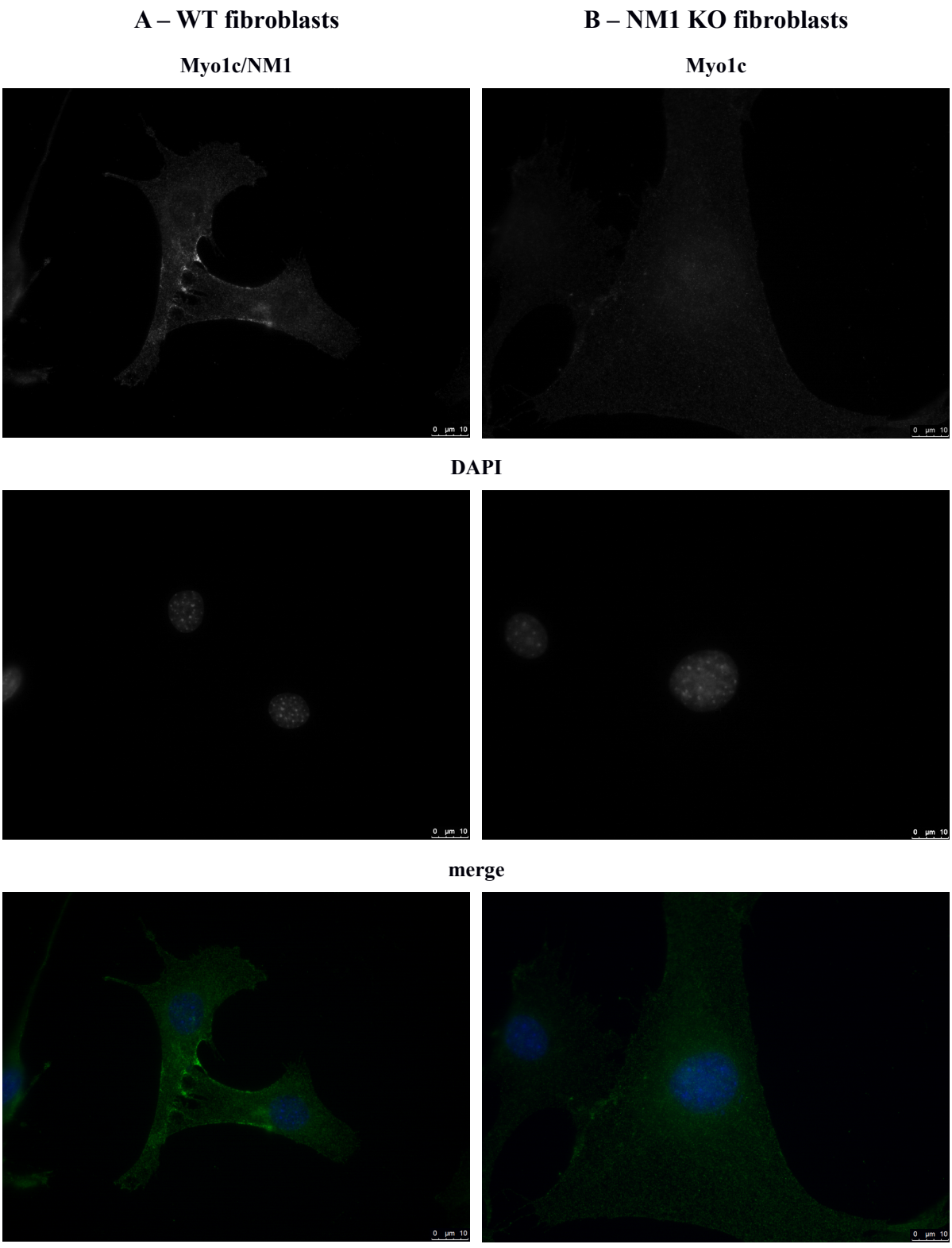

Figure 6.2. Cellular localization pattern of myosin 1c isoforms in mouse skin fibroblasts. (A) *WT fibroblasts show a typical membrane punctuated distribution of Myo1c/NM1 with discreet and highly localized peripheral patches of the fluorescence signal.* ***(B)*** *NM1 KO fibroblasts show an overall reduction of the plasma membrane fluorescence signal and, in particular, loss of the highly localized fluorescence patches at the cell periphery.*

NM1 has a similar localization pattern as Myo1c

Although originally considered as exclusively cytoplasmic or nuclear, it is now known that Myo1c participates in nuclear events and, conversely, NM1 is present in the cytoplasm as well, although their individual localization patterns in the cytoplasm are not completely overlapping (Dzijak et al., 2012; Venit et al., 2013, Venit and Kalendová, manuscript). Since we have been interested in possible roles of NM1 at the plasma membrane, we investigated the localization pattern of the NM1 protein in the cytoplasm and at the plasma membrane of U2OS cells and compared it to distribution of myosin 1c isoforms in control U2OS cells.

Immunofluorescence analysis of the cellular distribution of NM1 isoform in *MYO1C*-knockdown cells overexpressing NM1 from a lentiviral expression vector revealed that the overexpressed NM1 shows a pattern of fluorescence signal similar to the one observed in control U2OS cells. Specifically, we have found that individual NM1 displays a punctuated distribution at the plasma membrane, often with a particularly high localization at the cell periphery and in membrane protrusions (fig. 6.3B), a pattern typical for Myo1c as well (fig. 6.3A). This further supports the hypothesis that NM1 might be involved in membrane-related processes traditionally attributed to the Myo1c isoform.

Targeting of NM1 to the plasma membrane is PIP_2-dependent

Myo1c and other class I myosins specifically bind to the inositol ring of PIP_2 via pleckstrin homology (PH) motif in their tail domains and it has been suggested that the PH motif is responsible for the PIP_2-dependent anchoring of these proteins to the inner leaf of the cell membrane (Hokanson et al., 2006a; Hokanson et al., 2006b). However, it has been also shown that Myo1c protein contains three additional binding sites for PIP2 and other anionic phospholipids in the their calmodulin-binding IQ motifs which might represent an alternative mechanism of interaction between Myo1c and the plasma membrane (Hirono et al., 2004; Barylko et al., 2005). Thus, while the PIP_2-binding property of tail PH domain seems to be dominant for the membrane targeting of NM1/Myo1c, there might be additional mechanisms at play for the interaction of these proteins with plasma membrane.

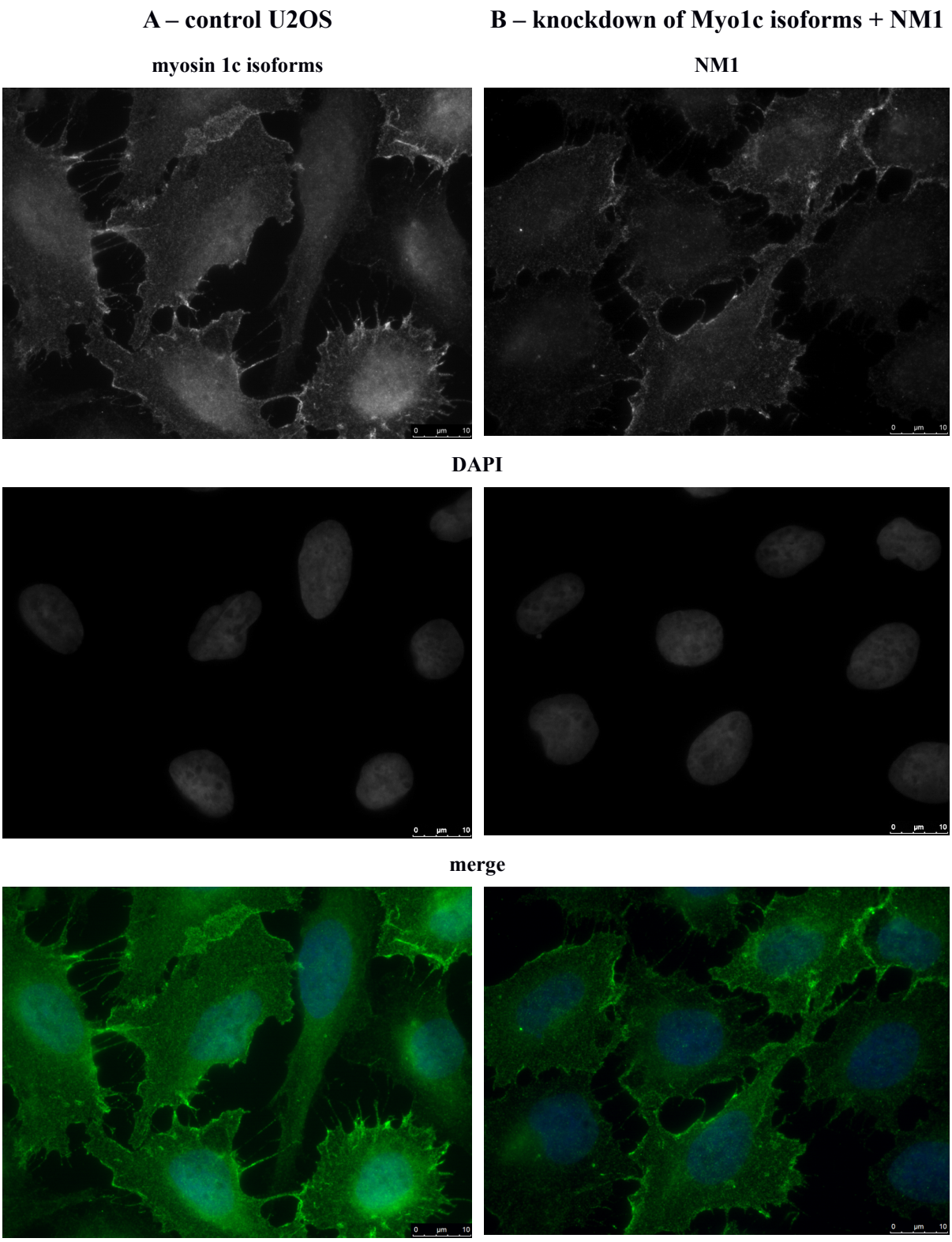

Figure 6.3. Cellular distribution pattern of the NM1 isoform in human U2OS cells. ***(A)*** *Control U2OS cells show a punctuated distribution of myosin 1c isoforms on the plasma membrane with a particularly high concentration at the cell periphery and in various cell membrane protrusions.* ***(B)*** *NM1 protein overexpressed in U2OS with all myosin 1c isoforms depleted by RNA interference shows a similar localization pattern as observed in control cells.*

Therefore, we decided to determine how NM1 interacts with plasma membranes in human U2OS cells and how it is targeted to its peripheral destinations. We transfected the *MYO1C*-knockdown cells with expression vectors carrying sequences of actin-binding and PIP_2-binding mutant variants of NM1 and compared their localization patterns. We have found that the disruption of the actin-binding site in the myosin head domain did not affect the targeting of NM1 to the plasma membrane and cell periphery, as the distribution pattern of the NM1 actin-binding mutant resembled that of the WT NM1 (fig. 6.4A). In a striking contrast, the mutation in the PIP_2-binding PH domain severely disrupted the targeting of NM1 to the cell edge and the protein remained diffused in the cytoplasm (fig. 6.4B).

Based on these observations we conclude that the PH domain of NM1 is responsible for its targeting and anchoring to the plasma membrane of U2OS cells and its localization at the cell periphery and membrane protrusions is PIP_2-dependent and not driven by actin.

Loss of NM1 leads to a significantly higher membrane elasticity

We showed previously that under strong hypotonic conditions, the survival rate of KO fibroblasts is higher than in case of WT cells and we have proposed that NM1 participates in the maintenance of cell membrane tension, as discussed in the Motivation chapter. However, a more direct approach was necessary to test this hypothesis and provide quantitative evidence supporting the role of NM1 in the regulation of cell membrane properties. Therefore, we decided to perform single-cell biomechanical measurements of individual mouse WT and NM1 KO skin fibroblasts using atomic force microscopy.

We have found that both WT and NM1 KO fibroblasts displayed a wide range of cellular morphologies, not indicating any morphological differences between both cell-lines (fig. 6.5A). Therefore, to achieve consistency in our measurements of membrane elasticity, we initially focused on regions of the cell surface directly above the nucleus (fig. 6.5B), which was a morphological feature clearly recognizable in all AFM scans of whole cells. For each cell, we gathered a set of force curves recorded in this region during AFM scanning, and a corresponding set of values of the Young's modulus of membrane elasticity (YM) was calculated (for more details see Materials and methods).

A – actin-binding NM1 mutant **B – PIP_2-binding NM1 mutant**

NM1

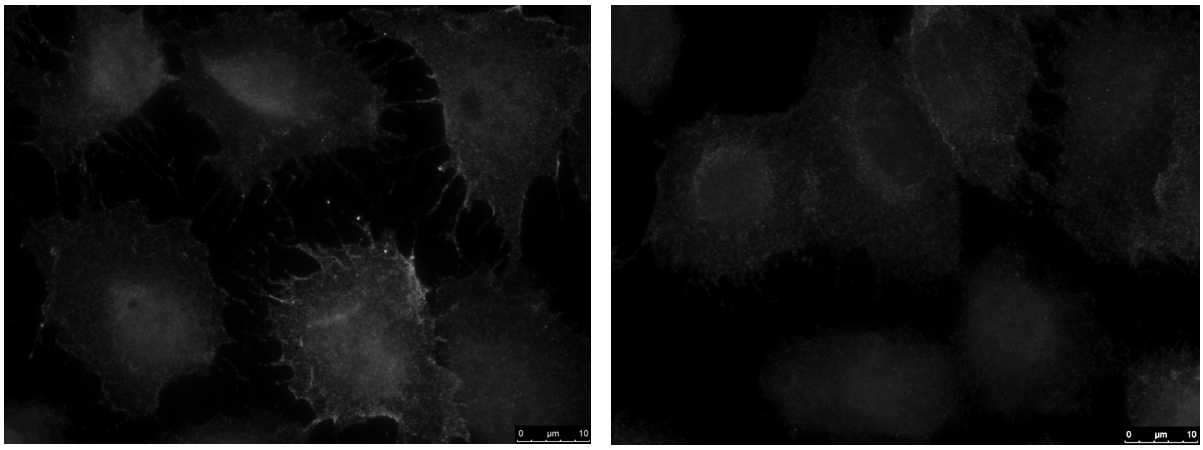

DAPI

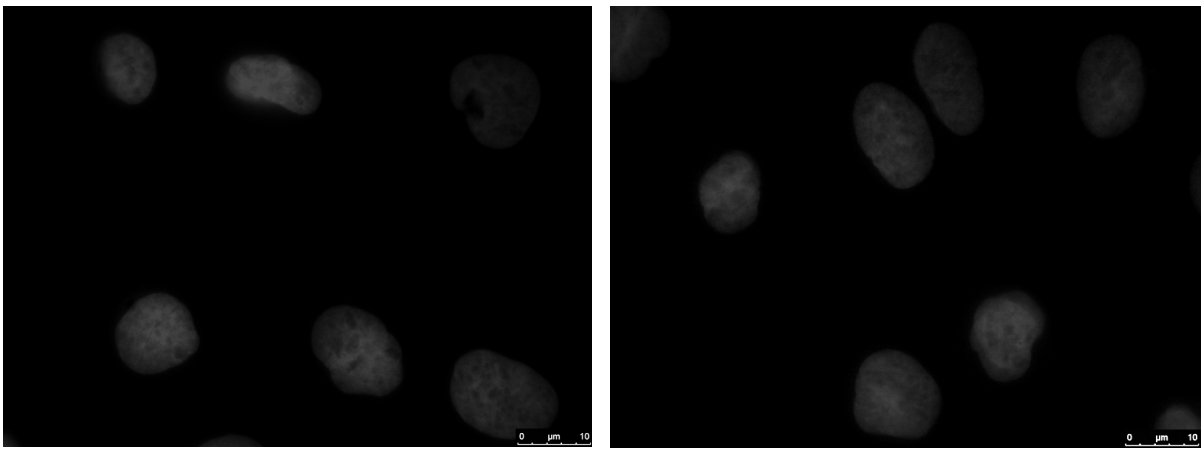

merge

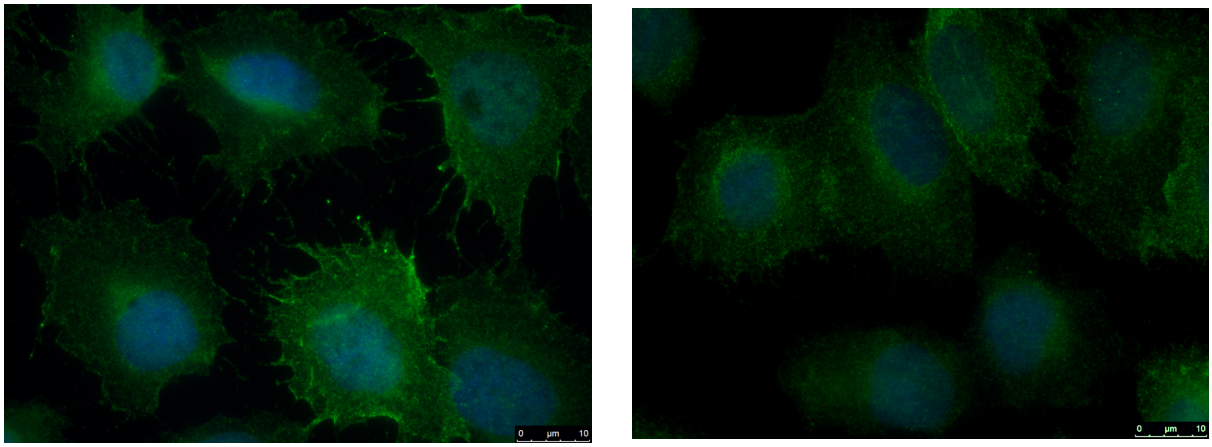

Figure 6.4. Cellular localization pattern of actin-binding and PIP_2-binding NM1 mutants. (A) *A disruption of the actin-binding site in the NM1 head domain did not affect the targeting of NM1 to the plasma membrane and cell periphery, as the distribution pattern of the NM1 actin-binding mutant resembles the pattern of WT NM1 shown in fig. 6.3.* ***(B)*** *Mutation in the PIP_2-binding PH domain disrupted the peripheral targeting of NM1 and the protein mostly remained diffused in the cytoplasm.*

Distribution plots of YM values calculated from each individual cell (fig. 6.6A) demonstrate that there was a striking difference in elasticities of WT and NM1 KO fibroblasts. WT cells show a wide range of elasticity phenotypes, represented by broad ranges of YM distributions of individual cells (fig. 6.6A, green boxplots). In contrast, values of elasticity modulus measured on NM1 KO cells show a consistently narrow distribution and are clustered predominately in the lower range of possible YM values (fig. 6.6A, red boxplots). Since lower values of YM correspond to higher elasticity of the sample and *vice versa* (Heu et al., 2012), these results indicate that while WT cells show a wide range of elastic phenotypes and, on average, appear to be more rigid, NM1 KO cells have a consistently higher membrane elasticity (fig. 6.6B). Overall, we have found that the average elasticity modulus is 0.77 MPa ± 0.38 MPa for WT cells and 0.29 ± 0.12 MPa for NM1 KO cells. This observed difference was verified using Student's *t*-test and was found to be statistically significant at the level of $p \leq 0.01$ (table 6.1).

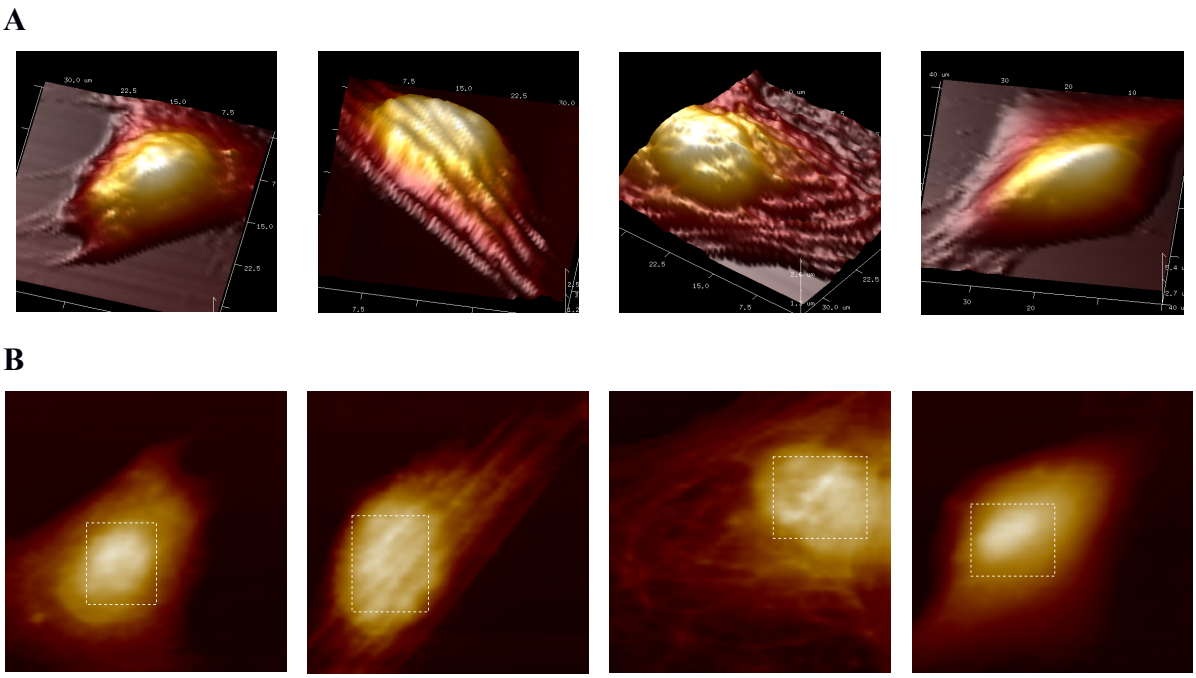

Figure 6.5. Different cell morphologies observed using AFM. (A) *3D reconstructions of mouse skin fibroblast surfaces showing a wide range of observed morphological features.* ***(B)*** *2D image height maps of cells displayed in (A). Highlighted areas represent examples of cell surface regions above the nucleus included in our analysis of membrane elasticity. Colors represent relative height values in each of the respective images (black – lowest, white – highest).*

A

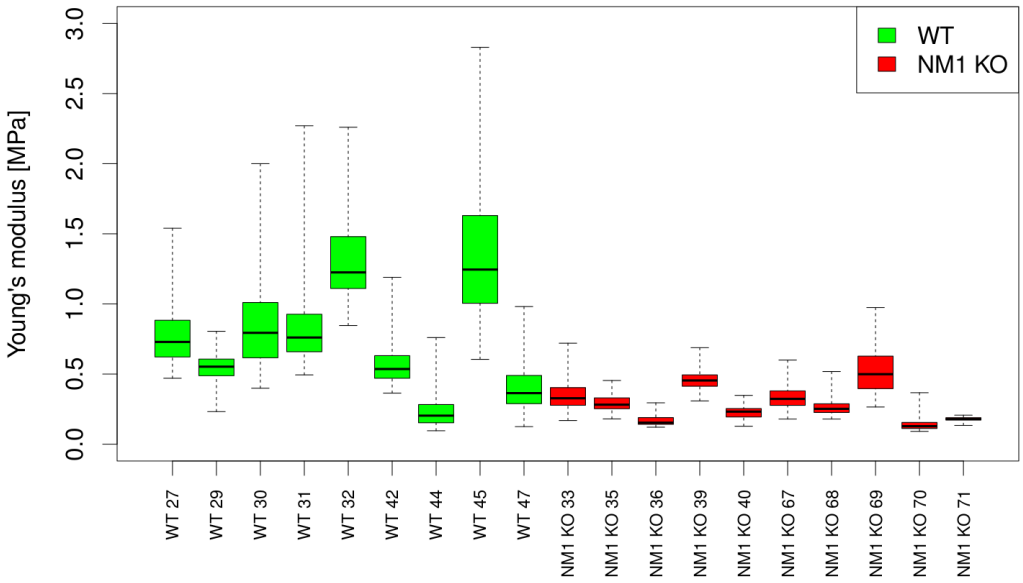

B

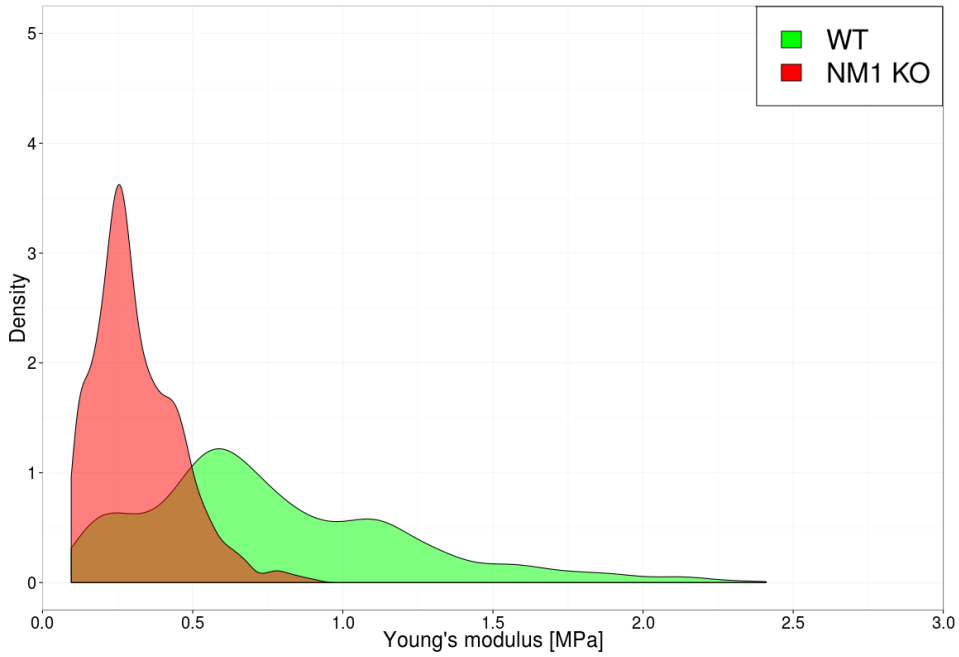

Figure 6.6. Distributions of YM values of WT and NM1 KO skin fibroblasts as measured over the cell surface above the nucleus. ***(A)*** *Values of YM measured above the nucleus of each individual WT and NM1 KO cell. WT cells show a wide range of elasticity phenotypes. In contrast, NM1 KO cells have a consistently high elasticity, represented by a narrow distribution of low YM values. Heights of boxes represent interquartile ranges, lines crossing the boxplots represent median values, whiskers extend to the most extreme lowest/highest values.* ***(B)*** *Density plots showing the overall distribution of YM values measured over the surfaces of all nine WT and ten NM1 KO cells, collected into two large datasets. Low value of YM means high elasticity, high value of YM represents higher rigidity and stiffness.*

		Young's modulus [MPa]										
		1	***2***	***3***	***4***	***5***	***6***	***7***	***8***	***9***	***10***	**overall**
WT	mean	0.78	0.55	0.83	0.86	1.32	0.57	0.25	1.34	0.41	-	0.77
	S.D.	0.21	0.10	0.26	0.32	0.29	0.14	0.14	0.45	0.17	-	0.38
NM1 KO	mean	0.35	0.29	0.17	0.46	0.23	0.33	0.27	0.52	0.15	0.18	0.29
	S.D.	0.10	0.06	0.05	0.07	0.04	0.08	0.07	0.16	0.05	0.01	0.12

Table 6.1. Means and standard deviations of YM values measured from WT and NM1 KO cells over the surface above the cell nucleus. *350 values of YM from nine individual WT and ten individual NM1 KO cells were included in the analysis, all measured over the plasma membrane region above the cell nucleus as shown in fig. 6.5B. The difference in the means of average YM of WT and NM1 KO cells was verified using Student's* t*-test and was found to be statistically significant at the level of* $p \leq 0.01$.

High elasticity of rescued NM1 KO cells is partially reversed to WT phenotype

In a control rescue experiment, we measured elasticities of the stable NM1 KO cell-line, expressing the exogenous NM1 protein from a lentiviral expression vector. Similarly to the previous experiment, we scanned the surfaces of seven rescued NM1 KO cells and for each cell, we gathered approximately 350 force-indentation curves from the surface region above the nucleus and calculated corresponding values of YM.

We have found that in contrast to NM1 KO cells, which showed a consistent narrow distribution of low values of YM (fig. 6.6), expression of the exogenous NM1 protein induced a partial reversal of this phenotype, causing a shift back towards the WT phenotype. Specifically, while several rescued NM1 KO cells still displayed a narrow elasticity and low standard deviation of the calculated elastic modulus, others appeared to be significantly more rigid and their elasticities were more varied, similarly to our observation of WT cells (table 6.2). Overall, we have found that the average value of Young's modulus of rescued NM1 KO cells was 0.57 MPa ± 0.27 MPa, which indicates a higher average cell stiffness than we

observed in NM1 KO cells (0.29 MPa ± 0.12 MPa). The overall difference in elasticities of both cell-lines was verified using Student's *t*-test and was found to be statistically significant at the level of $p \leq 0.05$. Moreover, in agreement with these results, when we combined the YM data measured from rescued NM1 KO cells into a single dataset and compared it with the overall results obtained from measurements of WT and NM1 KO cells, we have found that rescued NM1 KO cell-line shows an intermediate elastic phenotype (fig. 6.7).

Therefore, we concluded that the re-expression of NM1 in NM1 KO cells led to a partial recovery of the more elastically varied and, on average, more stiff phenotype that is characteristic for WT cells.

		Young's modulus [MPa]										
		1	***2***	***3***	***4***	***5***	***6***	***7***	***8***	***9***	***10***	**overall**
KO + NM1	mean	0.80	0.45	1.05	0.29	0.39	0.62	0.39	-	-	-	0.57
	S.D.	0.22	0.15	0.52	0.14	0.08	0.15	0.07	-	-	-	0.27
KO	mean	0.35	0.29	0.17	0.46	0.23	0.33	0.27	0.52	0.15	0.18	0.29
	S.D.	0.10	0.06	0.05	0.07	0.04	0.08	0.07	0.16	0.05	0.01	0.12

Table 6.2. Mean and standard deviation values of Young's modulus of rescued NM1 KO cells. *350 values of YM from seven rescued NM1 KO cells we included in the analysis, all measured over the plasma membrane region above the cell nucleus as shown in fig. 6.5B. Additionally, data measured on ten NM1 KO are shown for comparison. The difference in the means of average YM of both cell-lines was verified using Student's* t*-test and was found to be statistically significant at the level of* $p \leq 0.05$.

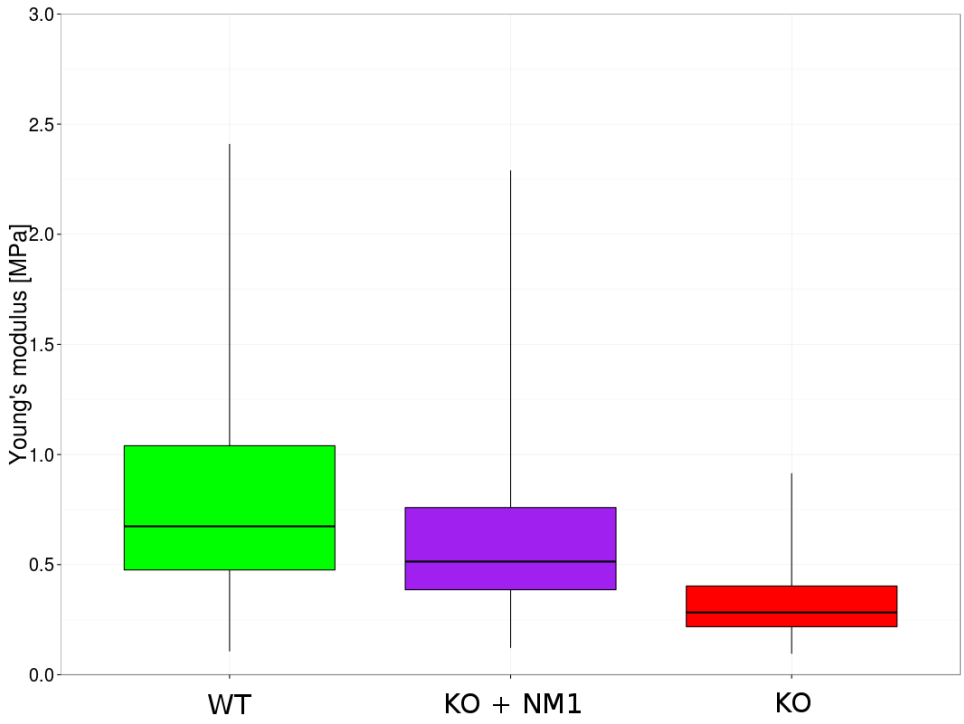

Figure 6.7. Distributions of values of Young's modulus in WT, rescued NM1 KO and NM1 KO cells. *YM data measured on seven rescued NM1 KO cells were collected together and plotted as a single data set. The overall distribution of all YM values measured on all WT and NM1 KO cells are shown for comparison. It can be seen that the rescued NM1 KO cell-line shows an intermediate phenotype with an apparent shift in the overall elasticity towards the more rigid and stiff WT phenotype. Heights of boxes represent interquartile ranges, lines crossing the boxplots represent median values, whiskers extend to the most extreme lowest/highest values.*

High elasticity of NM1 KO cells is uniform over the whole cell surface

NM1 is well known for its involvement in various nuclear functions (Pestic-Dragovich et al., 2000; Philimonenko et al., 2004; Percipalle et al., 2006; Cisterna et al., 2009; Obrdlik et al., 2010). Since we performed the previous experiments over the plasma membrane above the cell nucleus, we have decided to investigate the possibility that the observed changes in elastic properties of NM1 KO cell membranes are, in fact, caused by changes in the underlying cell nucleus. Therefore, we measured membrane elasticity of cells that were measured previously, but we focused on the plasma membrane region closer to the cell periphery, outside of the nuclear area (fig. 6.8).

We have found that values of YM calculated from individual NM1 KO cells cluster in the lower range of the YM spectrum in comparison to WT cells (table 6.3 and fig. 6.9) as was

observed in previous experiments performed above the cell nucleus (table 6.1 and fig. 6.6). The calculated mean value of YM for WT and NM1 KO cells was 0.94 MPa ± 0.47 MPa and 0.32 MPa ± 0.14 MPa, respectively, and the Student's *t*-test verified the statistical significance of this difference at the level of $p \leq 0.01$. Moreover, seven rescued NM1 KO cells again showed an intermediate overall elasticity, indicating that the expression of an exogenous NM1 partially restored the ability of cells to display wider range of elastic phenotypes and its higher average stiffness (fig. 6.10). Therefore, we conclude that the observed difference in membrane elasticities of NM1 KO and WT cells as measured above the cell nucleus is a feature of the plasma membrane itself and is not caused by structural changes in the nuclear compartment.

Furthermore, pair-wise comparison of results from individual NM1 KO cells revealed a remarkable similarity between YM distributions from measurements performed above the nucleus and outside the nuclear area, indicating that in both membrane regions, each NM1 KO cell had essentially the same elasticity (compare red boxplots in fig. 6.6A and fig. 6.9). In contrast, we have found that YM values measured in different regions of WT cells were often quite different, suggesting that membrane elasticities over the cell surface of these cells were variable (compare green boxplots in fig. 6.6A and fig. 6.9). One possible explanation for these observations is that while WT cells are able to modulate their membrane tension and elasticity, the absence of NM1 protein in NM1 KO fibroblasts disrupted the membrane tension regulatory mechanisms, causing a uniform distribution of high membrane elasticity over the whole cell surface.

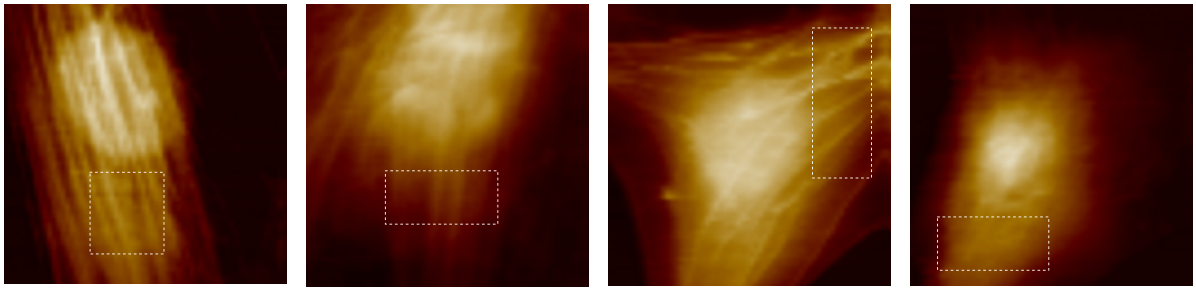

Figure 6.8. Examples of plasma membrane regions selected for the analysis of membrane elasticity closer to the cell periphery, outside the nuclear region. *Colors represent relative height values in each of the respective images (black – lowest, white – highest).*

		Young's modulus [MPa]										
		1	***2***	***3***	***4***	***5***	***6***	***7***	***8***	***9***	***10***	**overall**
WT	mean	1.19	0.45	1.78	1.24	0.35	0.66	1.02	0.87	-	-	0.94
	S.D.	0.47	0.08	0.27	0.31	0.10	0.17	0.43	0.16	-	-	0.47
KO	mean	0.26	0.30	0.20	0.51	0.24	0.40	0.25	0.62	0.20	0.22	0.32
	S.D.	0.04	0.04	0.04	0.07	0.06	0.06	0.03	0.11	0.06	0.03	0.14
KO + NM1	mean	1.10	0.45	1.47	0.36	0.71	0.73	0.47	-	-	-	0.75
	S.D.	0.26	0.21	0.32	0.28	0.16	0.15	0.05	-	-	-	0.4

Table 6.3. Mean and standard deviation values of Young's modulus of WT, NM1 KO and NM1 KO-rescued cells measured closer to the cell periphery. *350 values of YM from each individual cell were included in the analysis, all measured over the plasma membrane region closer to the cell periphery, as shown in fig. 6.8. The difference in the means of average YM of WT and NM1 KO cells was verified using Student's* t*-test and was found to be statistically significant at the level of* $p \leq 0.01$*. The difference in the means of average YM of rescued NM1 KO and NM1 KO cells was found to be statistically significant at the level of* $p \leq 0.05$*.*

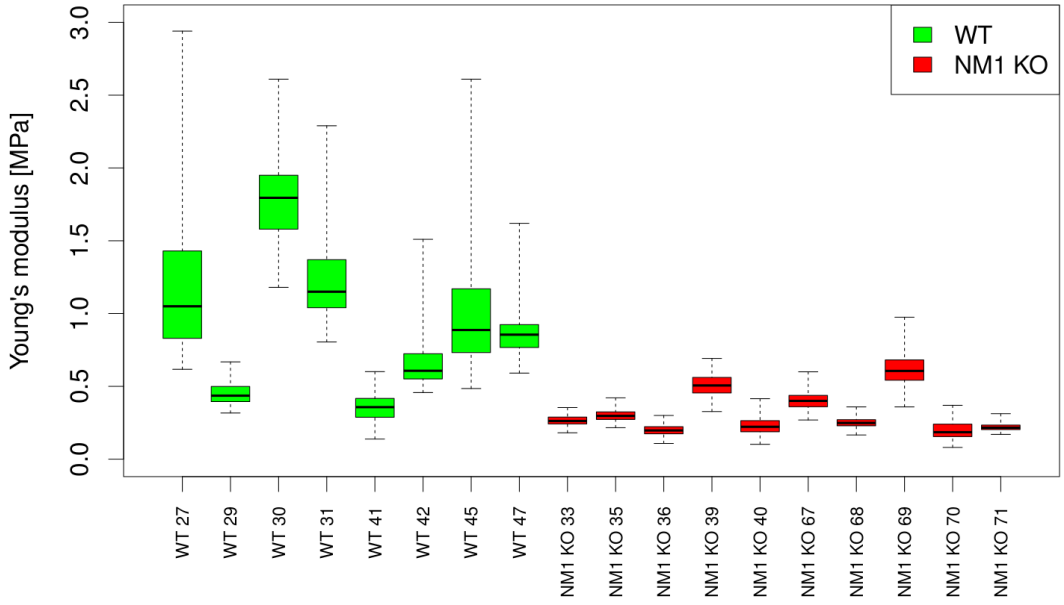

Figure 6.9. Distributions of YM values of individual WT and NM1 KO skin fibroblasts as measured closer to the cell periphery. *YM values were calculated from the cell surface region closer to the cell periphery as shown in fig. 6.8. Again, WT cells show a wide range of elasticity phenotypes. In contrast, NM1 KO cells have a consistently high elasticity, represented by a narrow distribution of low YM values. Heights of boxes represent interquartile ranges, lines crossing the boxplots represent median values, whiskers extend to the most extreme lowest/highest values. The set of WT cells included in this analysis is not entirely the same as in previous measurements because some AFM scan data were incomplete and had to be omitted.*

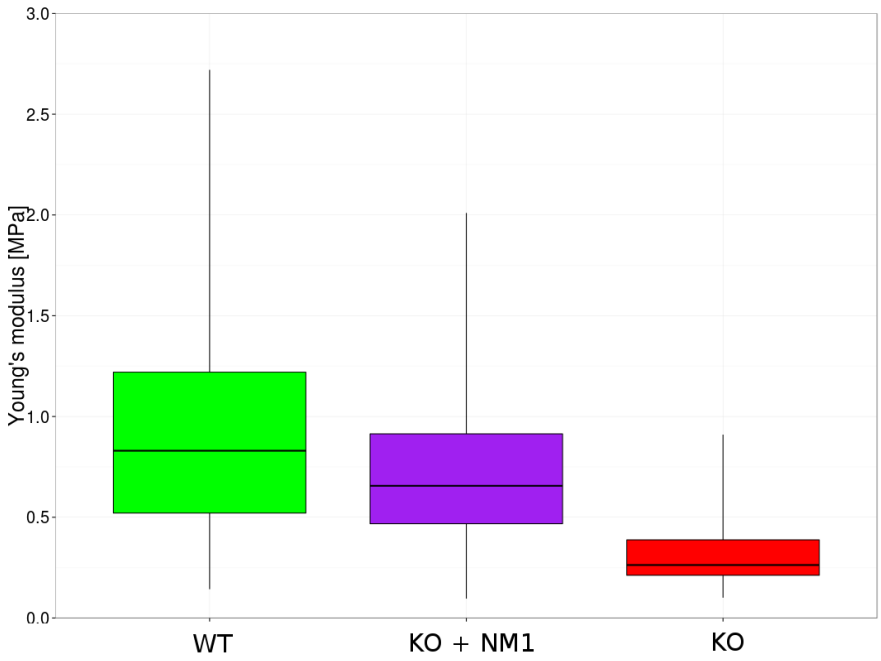

Figure 6.10. Elasticity distributions of WT, rescued NM1 KO and NM1 KO cells as measured closer to the cell periphery. *Boxplots show the overall trend in distribution of YM values measured over the surfaces of all WT, rescued NM1 KO and NM1 KO cells plotted as three large datasets. Rescued NM1 KO cells show an intermediate elastic phenotype, demonstrating a shift of the phenotype back towards WT. Height of boxes represent interquartile range, lines crossing the boxplots represent median values, whiskers extend to the most extreme lowest and highest values.*

Depletion of Myo1c isoforms in U2OS cells does not affect membrane properties

To get a further insight into the mechanism behind the involvement of *MYO1C* gene products in the maintenance of membrane tension and their potential differences, we decided to measure membrane elasticities of U2OS cells with a knockdown of all myosin 1c isoforms. Surprisingly, unlike in mouse skin fibroblasts, the measurements of five U2OS control cells and five cells depleted of all *MYO1C* gene products revealed no obvious changes in membrane elasticity of knockdown cells in comparison to control cells. In fact, as presented in fig. 6.11, distributions of values of YM measured from both cell-lines are strongly overlapping and we have found that the averages of mean elasticity modulus of knockdown and control U2OS cells was 24 kPa ± 12 kPa and 26 kPa ± 11 kPa, respectively, with no

statistically significant difference. This is in striking contrast to results obtained from measurements of mouse skin fibroblasts where the values of elasticity modulus of NM1 KO plasma membranes significantly differed from results obtained from WT cells (fig. 6.6).

In conclusion, while our results indicate that in mouse skin fibroblasts both NM1 and Myo1c significantly contribute to the maintenance of plasma membrane tension, other class I myosins might be more involved in the maintenance of membrane properties of human U2OS osteosarcoma cells (Nambiar et al., 2009). Finally, in agreement with this conclusion, hypotonic stress response test of *MYO1C*-knockdown U2OS cells did not reveal any differences in survival rates of these cells in comparison to control (data not shown).

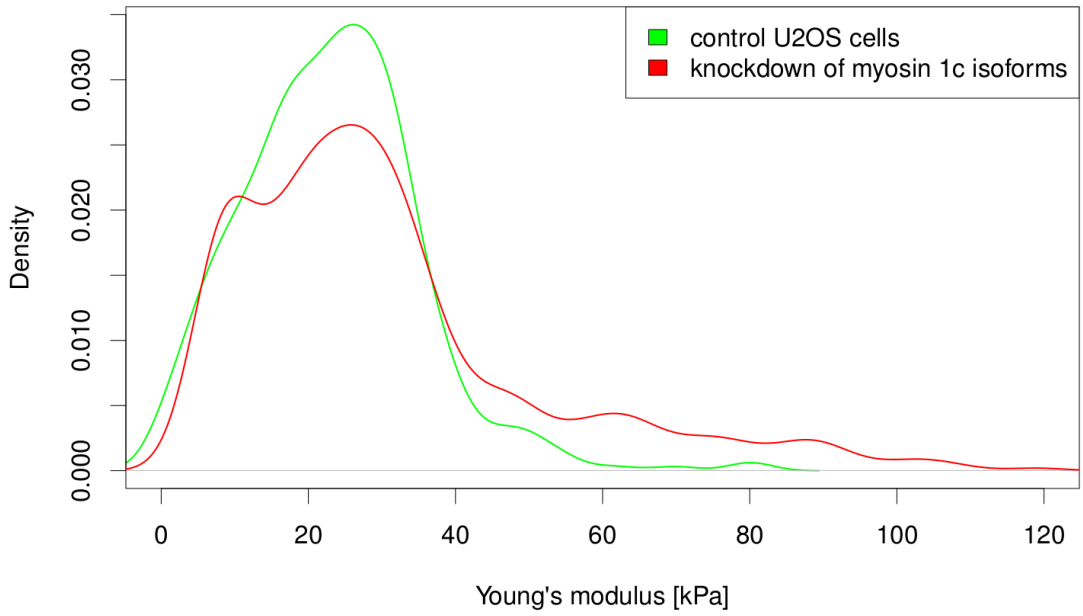

Figure 6.11. Results of elasticity measurements of U2OS cells performed over the surface above the cell nucleus. *Density plots showing the overall distribution of YM values measured on five control U2OS cells (green) and five cells with all myosin 1c isoforms depleted by RNA interference (red), plotted as two individual datasets. In contrast to previous measurements of mouse WT and NM1 KO skin fibroblasts, no difference in membrane elasticity has been observed between control and knockdown U2OS cell-lines.*

Knockout of NM1 has no effect on cell height

Based on previous results, we hypothesized that NM1 KO cells might be larger in size, mostly due to the partially loosened attachment of the cell membrane to the cortical actin cytoskeleton. However, it has proven impossible to calculate the exact volume of cells from AFM scan data, particularly because it was difficult to scan whole fibroblasts due to the wide diversity of their shapes and level of spreading. Instead, we have decided to measure and compare the highest points of ten WT and ten NM1 KO cells, using this parameter as an approximate measure of the overall cell height. For each scanned cell, we performed an *in silico* cross-section of the cell surface reconstructed from the AFM scan data, going through the highest part of each cell, and then automatically detected the highest points in all gathered cell section profiles using our custom made script (for more details see Materials and methods). An example of such cross section and cell profile curves with detected maximum heights are shown in fig. 6.12. Final results, summarized in fig. 6.13, indicate that there was no apparent difference between highest points of WT and NM1 KO cells. Indeed, both cell lines displayed a wide range of cell heights with the average being 2.2 ± 0.8 µm for WT and 2 ± 0.4 µm NM1 KO, which was not found to be statistically significant.

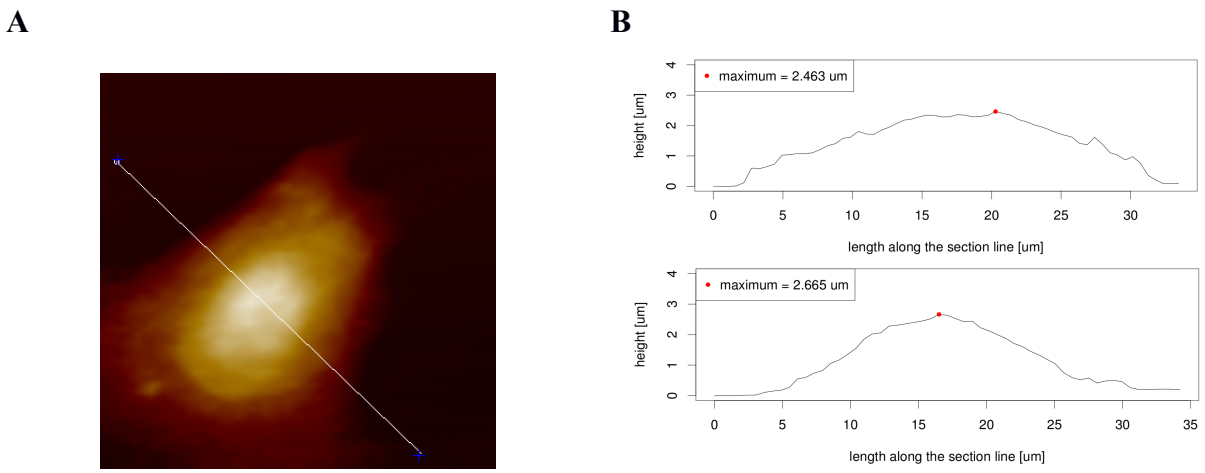

Figure 6.12. Detection of the highest point on the cell surface. (A) *An example of a cross-section performed* in silico *over two-dimensional image height map constructed from the AFM scan data. Colors represent relative height values (black – lowest, white – highest).* ***(B)*** *Examples of height profile curves constructed from cross sections of two respective cells. Red dots highlight the highest detected points included in the analysis.*

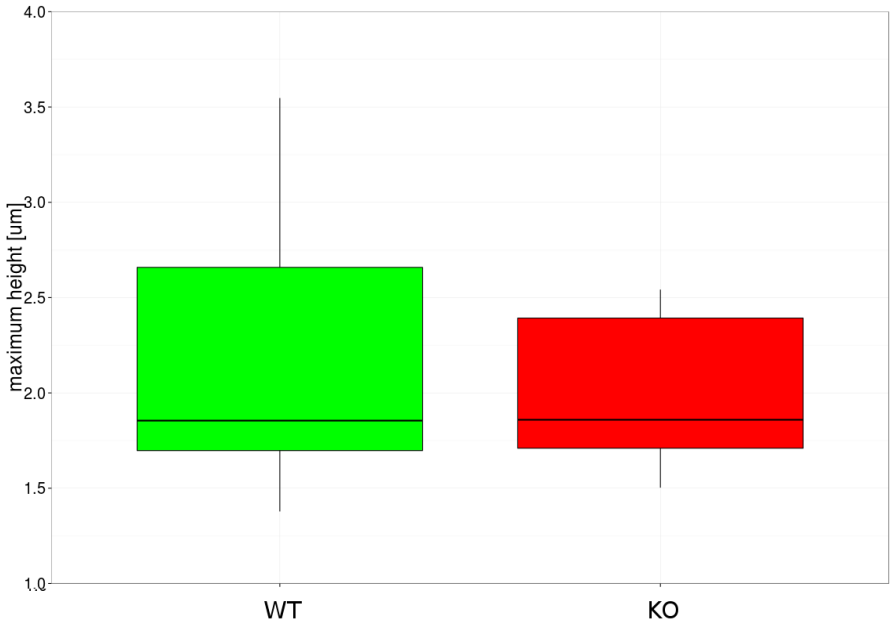

Figure 6.13. Comparison of the highest points of WT and NM1 KO skin fibroblasts. *The boxplots show an overall distributions of highest points in each respective cell-line. Height of a boxplot represents and interquartile range, line crossing the boxplot represent a median value, whiskers extend to the most extreme observed values.*

Membrane elasticity of NM1 KO cells shows a high degree of spatial homogeneity

To further expand our knowledge about distinct properties of NM1 KO and WT mouse fibroblasts and to get a more detailed insight into the reason behind their differences, we investigated the spatial distribution of values of the Young's modulus over the cell surface. We analyzed highly elastic NM1 KO cells and more stiff WT cells that showed various morphological features such as strong presence of actin stress fibers, as well as cells whose plasma membranes were completely smooth and without any apparent submembrane structures. Then, similarly as above, we focused our attention on membrane region above the cell nucleus, gathered a set of force-indentation curves in this region and calculated corresponding values of YM. Finally, we assigned each calculated value of YM to a specific position in a two-dimensional matrix according to the place on the cell surface where it was

measured and plotted this matrix as a two-dimensional image map of elasticity distribution (for more details see Materials and methods).

The results are summarized as in fig. 6.14 and fig. 6.15. In the first row, we show height maps of representative NM1 KO and WT cells together with highlighted membrane regions that were included in our analysis (fig. 6.14i, fig. 6.15i). As can be seen from 3D cell reconstructions (fig. 6.14ii, fig. 6.15ii), cells within both WT and NM1 KO cell-lines had different morphological features, such as smooth membrane surface (A), presence of visible stress fibers (B) and other intracellular, possibly nuclear, structures (C). In the third row, density plots of YM values calculated from highlighted areas of the cell surface are depicted (fig. 6.14iii, 6.15iii). In agreement with results reported above, it can be seen that a majority of YM values measured in individual NM1 KO cells cluster in a narrow range bellow 0.5 MPa which indicates a high membrane elasticity (fig. 6.14iii). In contrast, YM values measured on WT cells are distributed more broadly and are shifted in a direction towards higher membrane stiffness (fig. 6.15iii).

Finally, elasticity maps in the fifth row show that there are striking differences in spatial distributions of YM values measured from NM1 KO and WT cells. We have found that membranes of NM1 KO cells have a high degree of spatial homogeneity of low elasticity values, regardless of the presence or absence of intracellular structures (fig. 6.14iv). This is in agreement with narrowly clustered distributions of YM values in NM1 KO cells shown in histograms in fig. 6.14iii. Remarkably, in contrast to NM1 KO cells, plasma membranes of WT cells show a dramatically higher heterogeneity in the distribution of elastic properties, regardless the presence of structures under the cell membrane (fig. 6.15iv), which corresponds to a wide distribution of YM values revealed in WT cells (fig. 6.15iii) and suggests a broad distribution of NM1 over the plasma membrane.

Moreover, closer examination of elasticity maps from WT cell membranes revealed an intriguing correlation between the spatial pattern of YM distribution (fig. 6.15iv) and the presence of intracellular structures detectable from height and 3D images (fig. 6.15i, ii). We have found that the position and shape of these structures was clearly reflected in elasticity maps of WT membranes, indicating that their presence influenced the apparent membrane stiffness (fig. 6.15iv). This was in striking contrast to uniform and more homogeneous elasticity maps of NM1 KO membranes which have not shown a such a large influence from intracellular structures, if they were present (fig. 6.14iv). However, it should be noted that even though submembrane structures had an influence on the apparent elasticity of the WT cell membranes, the same structures did not have an effect on the observed mechanical

properties of NM1 KO cells.

In conclusion, this visual analysis of elasticity distribution allowed us to identify the distinct distribution patterns of membrane elasticity of NM1 KO and WT cells. Specifically, we have found that plasma membranes of NM1 KO cells have a highly homogeneous distribution of membrane elasticity regardless of the presence or absence of actin stress fibers or other submembrane structures. In contrast, spatial distribution of elasticity in WT cell membranes was more heterogeneous with a higher apparent stiffness and was partially affected by the presence of submembrane structures. However, since we observed higher elastic heterogeneity and membrane stiffness even WT cells with an apparently smooth surface, we conclude that for the overall plasma membrane stiffness of WT cells the presence of membrane-cytoskeleton NM1 linker is more important than the submembrane structures themselves.

Loss of NM1 has no detectable effect on cell shape or morphology

Previous studies provided evidence for the involvement of Myo1c in actin distribution at the cell periphery and it has been shown that its disruption has an adverse effects on cell spreading and maintenance of the cell shape (Maravillas-Montero et al., 2011; Brandstaetter et al., 2012). Therefore, we decided to investigate whether NM1 loss in the NM1 KO cells leads to an alteration in the actin distribution and cell shape.

Using an anti-actin antibody, we have detected a high concentration of actin bundles at the cell edge and membrane protrusions as well as a strong presence of actin stress fibers in the cytoplasm in both cell-lines (fig. 6.16). Moreover, both WT and NM1 KO cells displayed a wide range of cell shapes and morphologies typical for skin fibroblasts, not indicating any disruption in the mechanism of cell spreading or maintenance of the cell shapes caused by the loss of NM1. This was in agreement with our observations using AFM which revealed a wide range of morphological phenotypes of both cell-lines and suggests that in mouse fibroblasts, the contribution of NM1 protein in events related to the maintenance of cell shape, cell spreading and morphology is not significant enough to affect NM1 KO cells under standard conditions.

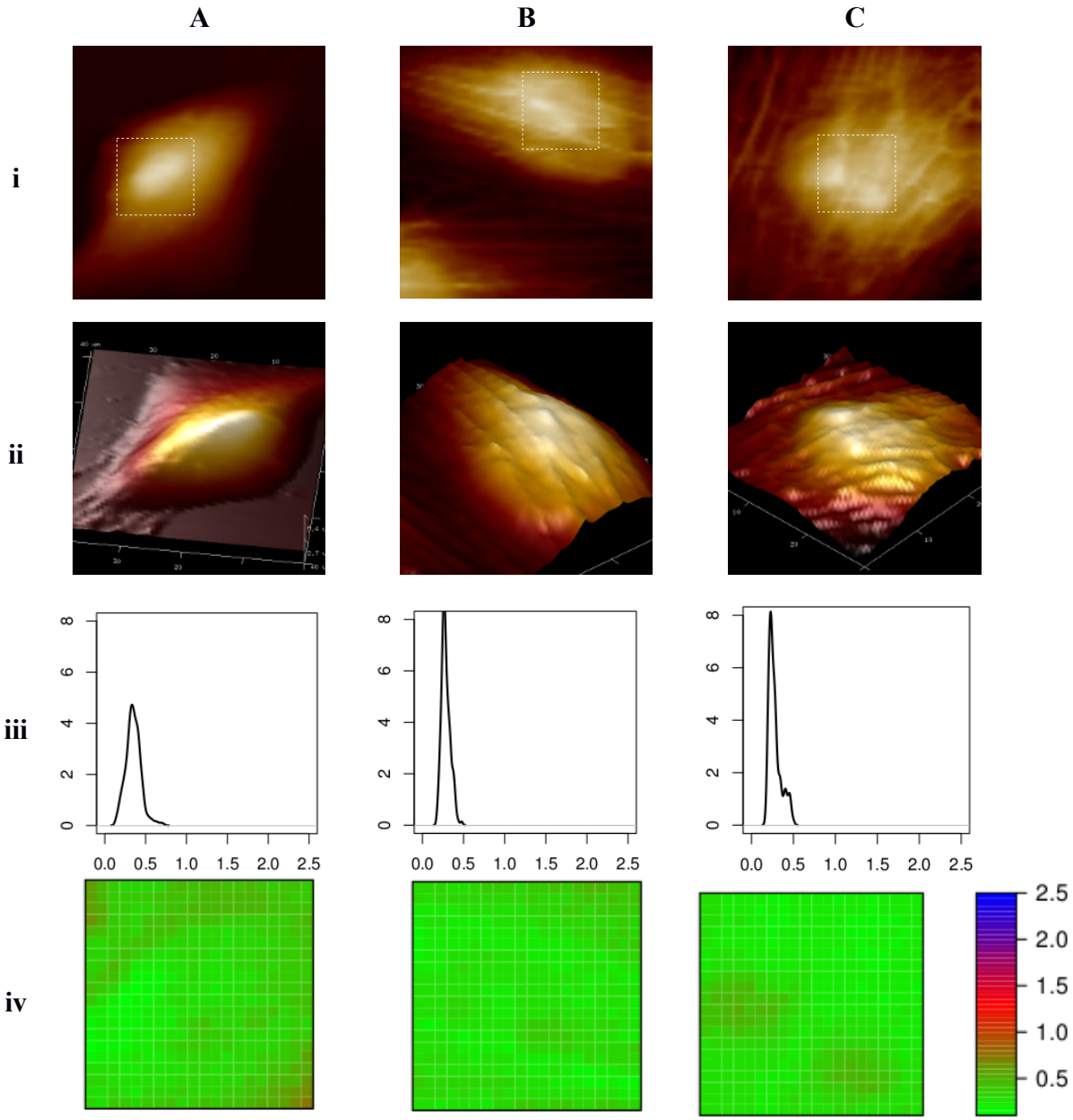

Figure 6.14 *Analysis of spatial distribution of Young's modulus over the NM1 KO cell surface.* ***Columns:*** ***(A)*** *NM1 KO cell with a smooth surface and no detectable submembrane structures.* ***(B)*** *NM1 KO cell with submembrane actin stress fibers.* ***(C)*** *NM1 KO cell with undefined intracellular structures.* ***Rows:*** ***(i)*** *2D height maps of cell topology with highlighted regions included in the elasticity measurements.* ***(ii)*** *3D AFM reconstructions of the cell surface.* ***(iii)*** *Density distribution plots of elasticity modulus calculated from regions highlighted in (i). Horizontal axis shows values of YM, vertical axis shows density values and have been omitted for space reasons.* ***(iv)*** *2D maps showing the spatial distribution of YM values over the selected cell surface region. Each pixel represents a single value of the YM and has been assigned color according to its position on the color scale. Colors in height maps and 3D reconstruction images represent relative height values in each of respective images (black – lowest, white – highest).*

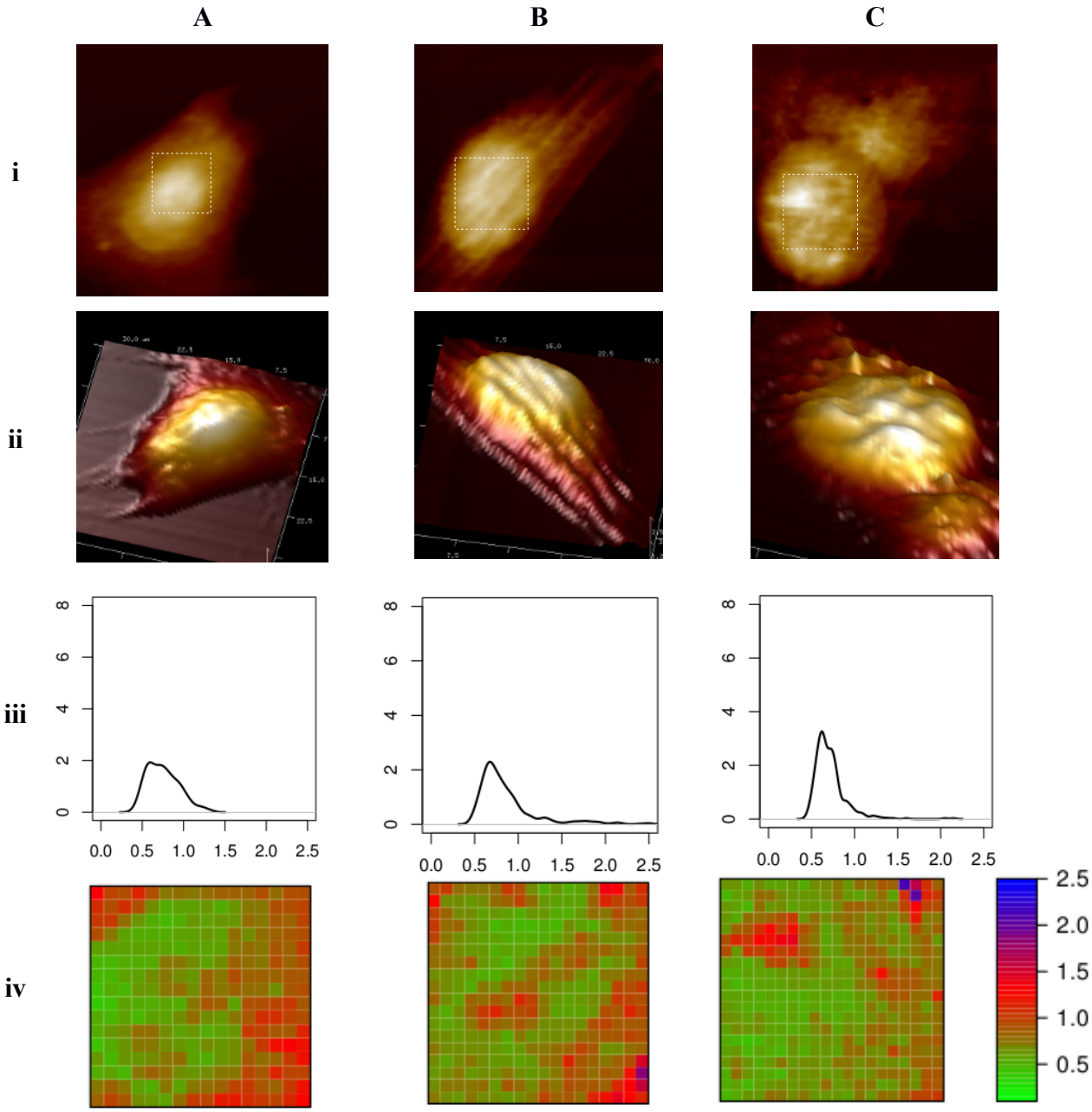

Figure 6.15 Analysis of spatial distribution of Young's modulus over the WT cell surface. Columns: ***(A)*** *WT cell with a smooth surface and no detected submembrane structures.* ***(B)*** *WT cell with submembrane actin stress fibers.* ***(C)*** *WT cell with undefined intracellular structures.* ***Rows: (i)*** *2D height maps of cell topology with highlighted regions included in the elasticity analysis.* ***(ii)*** *3D AFM reconstructions of the cell surface.* ***(iii)*** *Density distribution plots of elasticity modulus calculated from regions highlighted in (i). Horizontal axis shows values of YM, vertical axis shows density values and have been omitted for space reasons.* ***(iv)*** *2D maps showing the spatial distribution of YM values over selected cell surface region. Each pixel represents a single value of the YM and has been assigned color according to its position on the color scale. Colors in height maps and 3D reconstruction images represent relative height values in each of respective images (black – lowest, white – highest).*

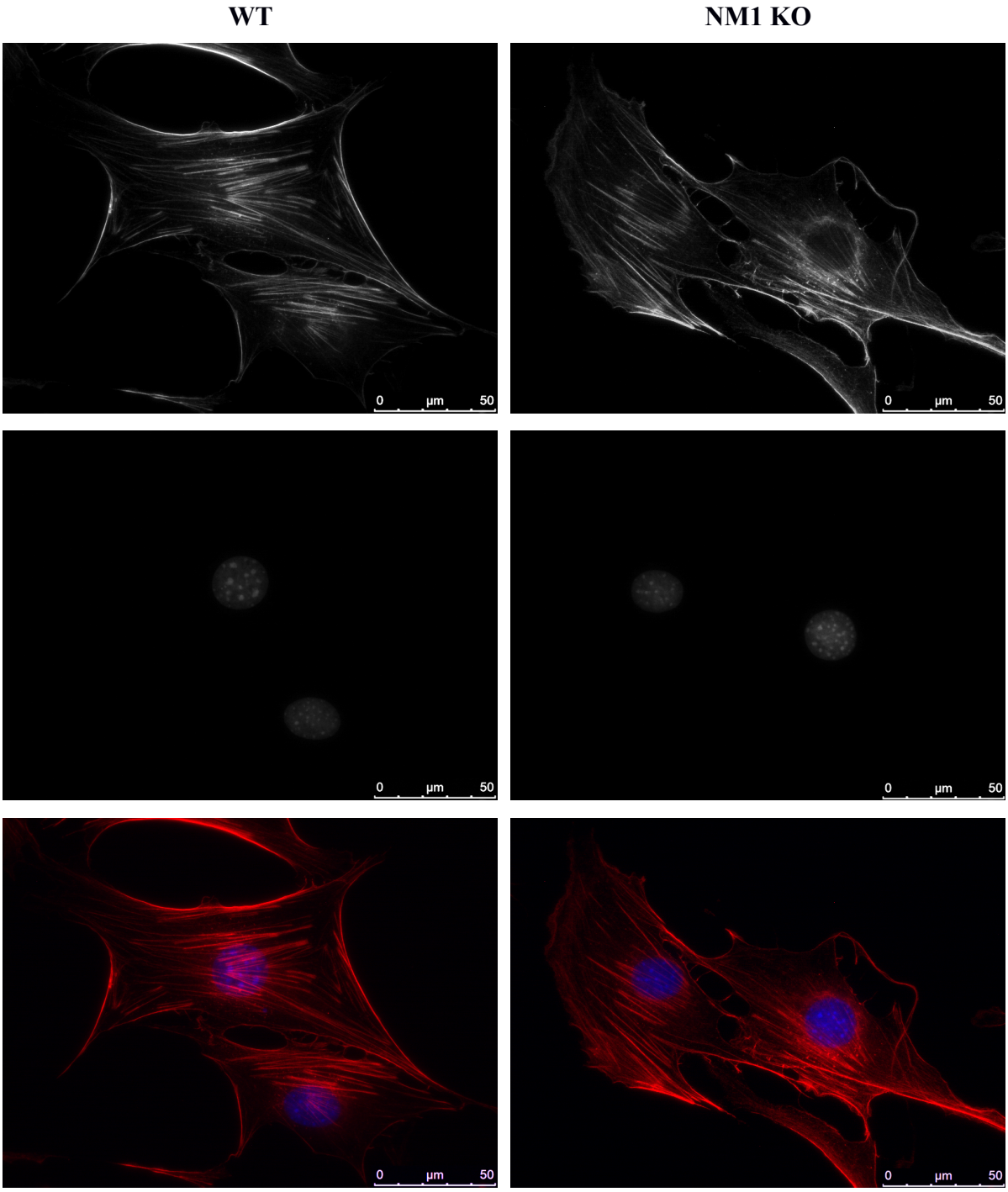

Figure 6.16 Comparison of actin distributions and cell shapes in WT and NM1 KO fibroblasts. *Both WT and NM1 KO cells showed a strong presence of actin fibers at the cell edges and in various cell membrane protrusions and displayed a wide range of cell shapes and morphologies typical for skin fibroblasts.*

7. Discussion

Myosin 1c (Myo1c), a molecular motor belonging to class I myosins (Odronitz and Kollmar, 2007), was the first unconventional myosin purified from mammalian tissues (Wagner et al., 1992). It has been shown to participate in a wide range of plasma membrane-related processes, including the regulation of tension-gated ion channels (Gillespie and Müller, 2009), exocytosis (Bose et al., 2004), endocytosis (Sokac et al., 2006), cell spreading and motility (Arif et al., 2011; Fan et al., 2012; Brandstaetter et al., 2012). All of these processes seem to be regulated by membrane tension (Diz-Muñoz et al., 2012) and relate to the ability of Myo1c to bind actin filaments and to directly interact with membrane phospholipids via their tail domains (Hokanson et al., 2006b). Moreover, it has been suggested that class I myosins, including Myo1c, can act as molecular force sensors, altering their biomechanical properties in response to changes in the applied mechanical load (Batters et al., 2004a; Batters et al., 2004b; Laakso et al., 2008). In agreement with this hypothesis, it has been shown that these proteins participate in the maintenance of membrane tension by serving as dynamic linkers mediating the interaction between the cell membrane and the underlying cortical actin network (Nambiar et al., 2009). Nuclear myosin 1 (NM1) is an isoform of Myo1c that has been extensively studied for its involvement in various nuclear processes such as transcription (Pestic-Dragovich et al., 2000; Philimonenko et al., 2004; Hofmann et al., 2006; Percipalle et al., 2006), chromatin remodeling (Percipalle et al., 2006) or maturation and export of small ribosomal subunits (Cisterna et al., 2009; Obrdlik et al., 2010). However, even though NM1 has been traditionally regarded as exclusively nuclear and Myo1c as purely cytoplasmic, recent studies done in our laboratory revealed that both NM1 and Myo1c participate in nuclear functions and that NM1 is present in the cytoplasm as well (Dzijak et al., 2012; Venit et al., 2013; Venit and Kalendová, manuscript). However, since the functional significance of this isoform outside the cell nucleus remained unknown, we have decided to investigate its role in the cytoplasm and at the plasma membrane.

NM1 localizes to the plasma membrane and cell periphery

Based on immunoflorescence staining using antibodies against a short N-terminal extension of NM1, earlier studies suggested that NM1 is an exclusively nuclear protein. However, testing of these antibodies in NM1 KO cells revealed cross-reactivity with unknown nuclear proteins, showing that the strong nuclear signal attributed previously to NM1 was not NM1-specific (unpublished data). This finding was further supported by fractionation experiments and western blotting showing that 60% of the total cellular pool of NM1/Myo1c proteins resides in the cytoplasm and that the ratio of both isoforms in nuclear and cytosolic compartments is roughly identical (Venit and Kalendová et al., manuscript).

Therefore, we used human U2OS cells overexpressing the NM1 protein and determined the localization pattern of NM1 protein in the cytoplasm using fluorescence microscopy. We have found that NM1 shows a uniformly distributed and punctuated membrane localization with a particularly strong enrichment in cell membrane protrusions all around the cell periphery, similarly to Myo1c staining (fig 6.1 and fig 6.3). Furthermore, immunofluorescence microscopy revealed that the actin-binding mutant of NM1 retains the ability to localize to the cell periphery and membrane protrusions (fig. 6.4A), which was in contrast to the PIP_2-binding NM1 mutant which lost the membrane and peripheral localization (fig. 6.4B). These results indicate that the membrane and peripheral targeting of NM1 is PIP_2-dependent and is not driven by actin.

Loss of NM1 leads to a significantly higher membrane elasticity of mouse skin fibroblasts

Our preliminary experiments showed that under hypotonic stress conditions, NM1 KO skin fibroblasts have a higher survival rate than WT cells. Based on the evidence supporting the role of class I myosins, including Myo1c, in maintenance of the plasma membrane–actin cytoskeleton interaction and in the regulation of the membrane tension (Nambiar et al., 2009), we have hypothesized that the NM1 protein possibly participates in this process as well. To test this hypothesis, we measured elastic properties of cell membranes of WT and NM1 KO mouse fibroblasts using atomic force microscopy.

Measurements of membrane elasticity performed above the cell nucleus revealed a significant difference between Young's modulus (YM) measured in WT (0.77 MPa ± 0.38

MPa) and NM1 KO (0.29 ± 0.12 MPa) fibroblasts (fig. 6.6, table 6.1), showing that the NM1 KO cell membranes are more elastic than in WT cells. Moreover, comparison of elasticity measurements revealed dramatically wider and more variable ranges in the YM distribution between individual WT cells (fig. 6.6A, green), which is in agreement with previous reports on wide range of YM and higher stiffness of healthy cells (Park et al., 2006; Cross et al., 2007; Cross et al., 2008). In a striking contrast, we have found that the overall membrane elasticities of individual NM1 KO fibroblasts fall into narrow range of YM values (fig. 6.6A, red).

These results were further confirmed by measurements performed all over the plasma membrane, not directly above the cell nucleus, but closer to the cell periphery. Therefore, the observed differences in WT and NM1 KO elasticities are not caused by some change in the nuclear structure in NM1 KO cells, but are exclusively attributed to changes in properties of the cell membrane itself. Moreover, pair-wise comparison of measurements performed above the nucleus and closer to the cell periphery revealed that while the elasticities of individual WT cells measured in both cell surface regions were often quite variable and different (fig. 6.6A and fig. 6.9, green), results from both regions in each individual NM1 KO cell were remarkably similar (fig. 6.6A and fig. 6.9, red). In conclusion, NM1 KO cells do not only show a significantly higher membrane elasticity, but this high degree of elasticity is uniformly preserved over the whole region of the cell surface, indicating a possible disruption of a membrane tension regulatory mechanisms in this cell-line.

Interestingly, our measurements of membrane elasticity in human osteosarcoma U2OS cells did not reveal any significant effect of knockdown of all myosin 1c isoforms on membrane elasticity (fig. 6.11), suggesting that while NM1 is an important regulator of the membrane tension in mouse fibroblasts, other class I myosins are likely to be more involved in the regulation of membrane tension of U2OS cells (Nambiar et al., 2009). Apparently, additional experiments in human U2OS cells will be necessary to test this hypothesis. Similarly, there appear to be no alterations in the distribution of actin filaments or cell spreading in NM1 KO fibroblasts. This suggests that in mouse skin fibroblasts, the contribution of NM1 in events related to the maintenance of cell shape and morphology is not large enough to affect NM1 KO cells, at least not under standard conditions.

Membrane elasticity of NM1 KO fibroblasts shows a high degree of spatial homogeneity

Finally, we computed visual maps of spatial distribution of individual YM values in NM1 KO and stiff WT cells. We have found that the elasticity maps of WT cell membranes show a heterogeneous distribution of a higher overall membrane stiffness with a certain level of influence from actin stress fibers and other submembrane structures (fig. 6.15iv). Importantly, elasticity maps of NM1 KO membranes had a more homogeneous distribution of high elasticity spots, regardless the presence or absence of submembrane structures (fig. 6.14iv). Therefore, although submembrane structures had a certain influence on the higher apparent stiffness of WT cell membranes, the same structures did not have a significant effect on the observed elasticity of NM1 KO cells. In conclusion, this suggests that the presence of the membrane-cytoskeleton NM1 linker is directly responsible for the the plasma membrane stiffness of WT cells in comparison to high elasticity of NM1 KO fibroblasts.

Nuclear myosin 1 is a regulator of plasma membrane tension

It has been shown previously that several class I myosins act as dynamic linkers, mediating the interaction between the cell membrane and the underlying cortical actin cytoskeleton, and thus contribute significantly to the regulation of the effective plasma membrane tension (Nambiar et al., 2009). In this study, we introduce a new and unexpected player into the spectrum of possible regulators of the plasma membrane tension and show that the loss of the NM1 protein, an isoform of Myo1c that has been traditionally regarded as exclusively nuclear, leads to a significant increase in the plasma membrane elasticity and decreases the membrane tension of mouse skin fibroblasts.

In conclusion, we present the following mechanistic model describing the molecular role of NM1 in the maintenance of membrane properties of these cells. We have found that individual NM1 KO fibroblasts show a similar level of high membrane elasticity which is kept consistent and uniform across their whole cell surface. In contrast, our measurements of individual WT fibroblasts revealed dramatically wider and more variable ranges of elasticity of the plasma membrane. Earlier AFM studies revealed that for indentation depths up to 500 nm, which was an approximate maximal indentation depth in our study as well, cortical actin filaments are predominately responsible for the observed elastic properties of cells (Rotsch

and Radmacher, 2000; Kasas et al., 2005). Therefore, we suggest that the uniformly high elasticity observed in NM1 KO skin fibroblasts, which completely lack the NM1 protein, represents a certain baseline level of the lowest membrane tension maintained in these cells by other class I myosins linking plasma membrane to the underlying cortical actin cytoskeleton (Nambiar et al., 2009), regardless of their motile or metabolic state or their position in the cell-cycle. Therefore, we propose that the NM1 protein participates in the maintenance of an effective plasma membrane tension by serving as an additional, regulatory linker, allowing the cell to decrease the elasticity of the plasma membrane and increase its effective tension, according to its specific needs.

In conclusion, we have brought evidence showing for the first time that the nuclear myosin 1 has a direct functional role in the cytoplasm as a dynamic linker between the cell membrane and the underlying cortical actin cytoskeleton, regulating the degree of an effective plasma membrane tension.

Possible clinical relevance of the NM1 KO phenotype

Interestingly, while we have found that skin fibroblasts derived from the NM1 KO mice show a significant decrease in the membrane tension, which appears to be an important regulator of a wide range of critical cellular processes (Diz-Muñoz et al., 2012), no related defects were found by phenotypic screening of the NM1 KO mice. This can be explained by the fact that the plasma membrane tension is maintained by several class I myosins (Nambiar et al., 2009) and, therefore, the disruption of one of them does not necessarily cause a defective phenotype, unless we put cells under stress conditions such as hypotonic environment. Moreover, a large number of studies have reported that cancer cells show a significantly higher elasticity and deformability than control cells derived from healthy tissues (Lekka et al., 1999; Guck et al., 2005; Cross et al., 2007; Cross et al., 2008; Faria et al., 2008; Li et al., 2008; Remmerbach et al., 2009; Lekka et al., 2012a). In fact, it has been shown that the altered elastic phenotype of cancer cells alone is so specific and unique, that it might serve as a marker to specifically distinguish between tumor and healthy cells in mixed cultures (Lekka et al., 2012b). Interestingly, it has been also reported that while healthy control cells display a more broad distribution of the elasticity modulus, characterized by a wide log-normal distribution function (fig. 7.1A), cancer cells show a significantly more narrow features of the normal Gaussian distribution with a significantly lower standard deviation of the Young's

modulus (fig. 7.1C) (Cross et al., 2007; Cross et al., 2008). Interestingly, these results closely resemble our observations of elastic phenotypes of WT and NM1 KO cells, which have shown very similar relative patterns of distribution of Young's modulus values (fig. 7.1B and fig. 7.1D). Therefore, we suggest that a deletion or mutation of the NM1 protein might lead to an increased metastatic potential of these cells.

It has been proposed that the higher elasticity and deformability of metastatic cells allows them to move through extracellular tissues more efficiently, thus effectively increasing their metastatic potential (Park et al., 2005; Darling et al., 2007; Remmerbach et al., 2009). Indeed, decrease in the plasma membrane tension has been linked to an increased lamellipodial extension and cell motility (Raucher and Sheetz, 2000; Houk et al., 2012). In this regard, since we have provided a direct evidence for the significant decrease of membrane tension in NM1 KO skin fibroblasts, we suggest that the disruption of the NM1 protein might increase their deformability, which could lead to an increased susceptibility to metastatic cancer. However, a more functional approach, directly measuring the migration potential of WT and NM1 KO cells of various cell types and their ability to invade through the three-dimensional space of extracellular matrix will be necessary to verify our hypothesis.

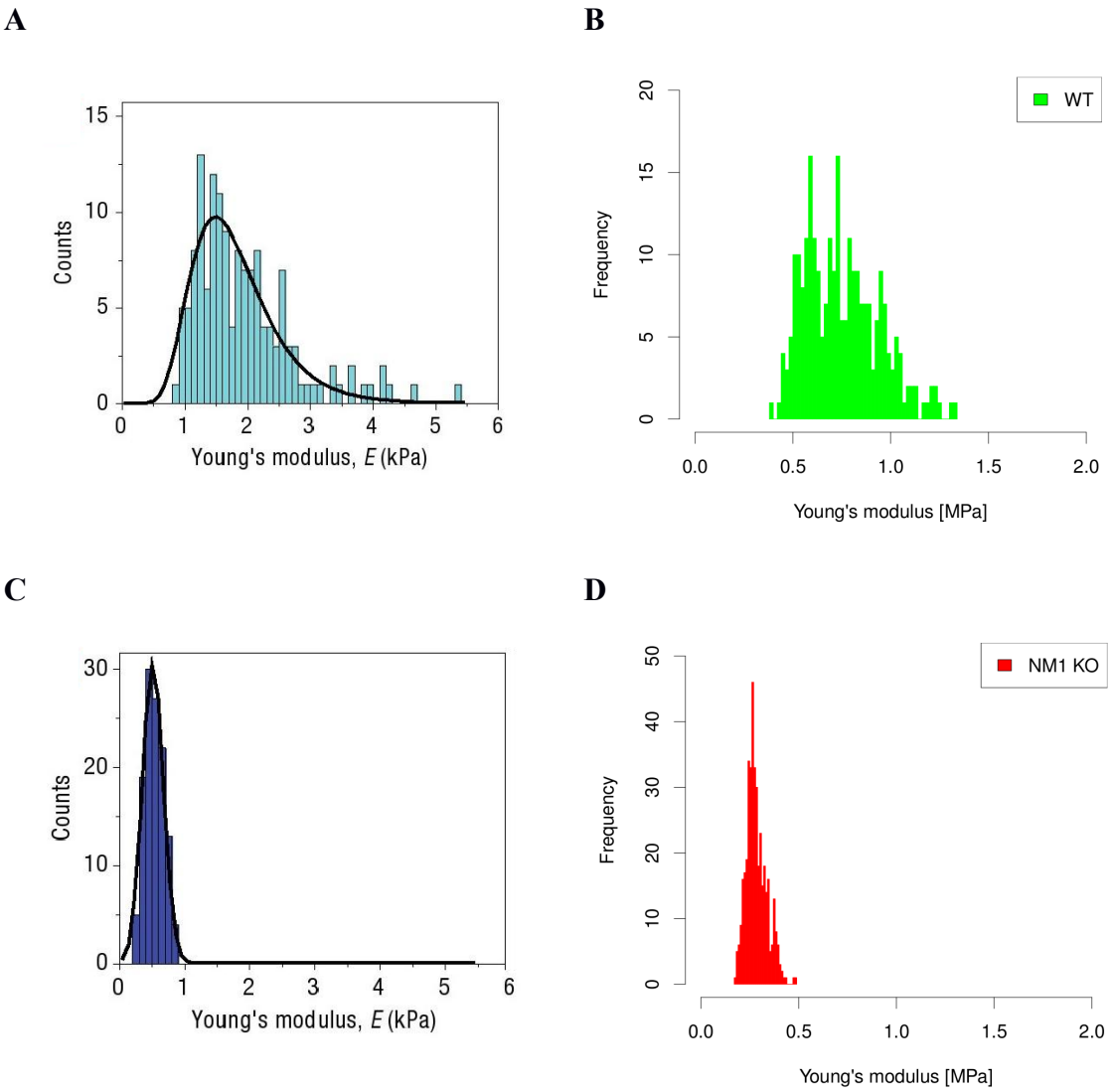

Figure 7.1 Comparison of histograms showing distribution of Young's modulus values measured in clinical samples and mouse skin fibroblasts. (A) *YM distribution characteristic for healthy cells, fitted with a log-normal curve.* ***(B)*** *Distribution of YM values measured from a WT mouse skin fibroblast.* ***(C)*** *YM distribution characteristic for cancer cells, fitted with a Gaussian curve.* ***(D)*** *Distribution of YM values measured from NM1 KO mouse skin fibroblast. Note, that there is a similar relative difference between YM distributions measured in healthy/cancer cells and WT/NM1 KO fibroblasts. Plots in (A) and (C) were taken and adapted from Cross et al., 2007. The difference between absolute YM values measured in (A), (C) and (B), (D) can be explained by different experimental conditions and different AFM equipment used in each study. YM is extremely sensitive to changes in various experimental conditions and can be used only as a relative measure of sample elasticity unless all experimental conditions are preserved between experiments (Lekka et al., 2012b).*

8. Summary

Nuclear myosin 1 (NM1) has a similar localization pattern as myosin 1c (Myo1c) and other class I isoforms.

NM1 localizes to the plasma membrane and shows a uniform punctuated distribution pattern with a particularly high concentration at the cell periphery and in various plasma membrane protrusions, which is typical for other class I myosins as well.

The localization of NM1 to the cell periphery is PIP_2-dependent and is not driven by actin.

Actin-binding NM1 mutant retains the peripheral localization pattern typical for myosin 1c isoforms. In contrast, mutation of the PIP_2-binding site in the NM1 tail domain abolishes its localization to the plasma membrane and the protein remains diffused in the cytoplasm.

NM1 acts as a regulator of the plasma membrane tension in mouse fibroblasts

Atomic force microscopy (AFM) measurements of plasma membrane elasticity revealed that the loss of the NM1 isoform leads to a significantly higher membrane elasticity of mouse NM1 KO skin fibroblasts in comparison to WT cells. Moreover, while WT fibroblasts are able to show a wide range of different elastic phenotypes, NM1 KO cells show a consistently narrow range of membrane elasticity.

Myosin 1c isoforms do not appear to play a major regulatory role in the maintenance of plasma membrane tension in human osteosarcoma cells.

AFM measurements of U2OS cells with all myosin 1c isoforms depleted by RNA interference did not reveal a significant change of membrane elasticity in comparison to control cells. Therefore, the tension maintenance function of myosin 1c isoforms in these cells is possibly fulfilled to a greater extent by other class I myosins.

Morphology and spreading of mouse fibroblasts is not affected by the loss of NM1

Comparison of cell heights calculated from the AFM scan data revealed that both WT and NM1 KO fibroblast cells have comparable cell heights. Similarly, there appear to be no alterations in the distribution of actin filaments or spreading of NM1 KO cells. This suggests that in mouse fibroblasts, the contribution of NM1 in events related to the maintenance of cell shape and morphology is not large enough to affect NM1 KO cells under standard conditions.

References

Akhmanova A, Hammer JA 3rd. Linking molecular motors to membrane cargo. 2010. *Curr Opin Cell Biol*. **22**: 479-87. Review.

Arif E, Wagner MC, Johnstone DB, Wong HN, George B, Pruthi PA, Lazzara MJ, Nihalani D. 2011. Motor protein Myo1c is a podocyte protein that facilitates the transport of slit diaphragm protein Neph1 to the podocyte membrane. *Mol Cell Biol*. **31**: 2134-50.

Barylko B, Wagner MC, Reizes O, Albanesi JP. 1992. Purification and characterization of a mammalian myosin I. *Proc Natl Acad Sci U S A.* **89**: 490-4.

Barylko B, Jung G, Albanesi JP. Structure, function, and regulation of myosin 1C. 2005. *Acta Biochim Pol.* **52**: 373-80. Review.

Batters C, Arthur CP, Lin A, Porter J, Geeves MA, Milligan RA, Molloy JE, Coluccio LM. 2004a. Myo1c is designed for the adaptation response in the inner ear. *EMBO J*. **23**: 1433-40.

Batters C, Wallace MI, Coluccio LM, Molloy JE. 2004b. A model of stereocilia adaptation based on single molecule mechanical studies of myosin I. *Philos Trans R Soc Lond B Biol Sci.* **359**: 1895-905.

Berquand A. 2012. Quantitative Imaging of Living Biological Samples by PeakForce QNM Atomic Force Microscopy. Bruker *Application Note*. **135**.

Binnig G, Quate CF, Gerber C. 1986. Atomic force microscope. *Phys Rev Lett*. **56**: 930-933.

Bond LM, Brandstaetter H, Kendrick-Jones J, Buss F. 2013. Functional roles for myosin 1c in cellular signaling pathways. *Cell Signal.* **25**: 229-35. Review.

Bose A, Guilherme A, Robida SI, Nicoloro SM, Zhou QL, Jiang ZY, Pomerleau DP, Czech MP. 2002. Glucose transporter recycling in response to insulin is facilitated by myosin Myo1c. *Nature*. **420**: 821-4.

Bose A, Robida S, Furcinitti PS, Chawla A, Fogarty K, Corvera S, Czech MP. 2004. Unconventional myosin Myo1c promotes membrane fusion in a regulated exocytic pathway. *Mol Cell Biol.* **24**: 5447-58.

Brandstaetter H, Kendrick-Jones J, Buss F. 2012. Myo1c regulates lipid raft recycling to control cell spreading, migration and Salmonella invasion. *J Cell Sci.* **125**: 1991-2003.

Bridgman PC, Dave S, Asnes CF, Tullio AN, Adelstein RS. 2001. Myosin IIB is required for growth cone motility. *J Neurosci.* **21**: 6159-69.

Butt HJ. 1991. Measuring electrostatic, van der Waals, and hydration forces in electrolyte solutions with an atomic force microscope. *Biophys J.* **60**: 1438-44.

Chuang CH, Carpenter AE, Fuchsova B, Johnson T, de Lanerolle P, Belmont AS. 2006. Long-range directional movement of an interphase chromosome site. *Curr Biol.* **16**: 825-31.

Cisterna B, Malatesta M, Dieker J, Muller S, Prosperi E, Biggiogera M. 2009. An active mechanism flanks and modulates the export of the small ribosomal subunits. *Histochem Cell Biol.* **131**: 743-53.

Cope MJ, Whisstock J, Rayment I, Kendrick-Jones J. 1996. Conservation within the myosin motor domain: implications for structure and function. *Structure*. **4**: 969-87.

Cross SE, Jin YS, Rao J, Gimzewski JK. 2007. Nanomechanical analysis of cells from cancer patients. *Nat Nanotechnol.* **2**: 780-3.

Cross SE, Jin YS, Tondre J, Wong R, Rao J, Gimzewski JK. 2008. AFM-based analysis of human metastatic cancer cells. *Nanotechnology*. **19**: 384003.

Darling EM, Zauscher S, Block JA, Guilak F. 2007. A thin-layer model for viscoelastic, stress-relaxation testing of cells using atomic force microscopy: do cell properties reflect metastatic potential? *Biophys J.* **92**: 1784-91.

De La Cruz EM, Ostap EM. Relating biochemistry and function in the myosin superfamily. 2004. *Curr Opin Cell Biol*. **16**: 61-7. Review.

Diz-Muñoz A, Fletcher DA, Weiner OD. 2013. Use the force: membrane tension as an organizer of cell shape and motility. *Trends Cell Biol.* **23**: 47-53. Review.

Domke J, Radmacher M. 1998. Measuring the elastic properties of thin polymer films with the atomic force microscope. *Langmuir*. **14**: 3320–25.

Dufrêne YF, Martínez-Martín D, Medalsy I, Alsteens D, Müller DJ. 2013. Multiparametric imaging of biological systems by force-distance curve-based AFM. *Nat Methods.* **10**: 847-54. Review.

Dzijak R, Yildirim S, Kahle M, Novák P, Hnilicová J, Venit T, Hozák P. 2012. Specific nuclear localizing sequence directs two myosin isoforms to the cell nucleus in calmodulin-sensitive manner. *PLoS One*. **7**: e30529.

Fan Y, Eswarappa SM, Hitomi M, Fox PL. 2012. Myo1c facilitates G-actin transport to the leading edge of migrating endothelial cells. *J Cell Biol*. **198**: 47-55.

Faria EC, Ma N, Gazi E, Gardner P, Brown M, Clarke NW, Snook RD. 2008. Measurement of elastic properties of prostate cancer cells using AFM. *Analyst*. **133**: 1498-500.

Fischer S, Windshügel B, Horak D, Holmes KC, Smith JC. 2005. Structural mechanism of the recovery stroke in the myosin molecular motor. *Proc Natl Acad Sci U S A*. **102**: 6873-8.

Fomproix N, Percipalle P. 2004. An actin-myosin complex on actively transcribing genes. *Exp Cell Res*. **294**: 140-8.

Foth BJ, Goedecke MC, Soldati D. 2006. New insights into myosin evolution and classification. *Proc Natl Acad Sci U S A*. **103**: 3681-6.

Gillespie PG, Albanesi JP, Bahler M, Bement WM, Berg JS, Burgess DR, Burnside B, Cheney RE, Corey DP, Coudrier E, de Lanerolle P, Hammer JA, Hasson T, Holt JR, Hudspeth AJ, Ikebe M, Kendrick-Jones J, Korn ED, Li R, Mercer JA, Milligan RA, Mooseker MS,

Ostap EM, Petit C, Pollard TD, Sellers JR, Soldati T, Titus MA. 2001. Myosin-I nomenclature. *J Cell Biol*. **155**: 703-4.

Gillespie PG, Müller U. 2009. Mechanotransduction by hair cells: models, molecules, and mechanisms. *Cell*. **139**: 33-44. Review.

Guck J, Schinkinger S, Lincoln B, Wottawah F, Ebert S, Romeyke M, Lenz D, Erickson HM, Ananthakrishnan R, Mitchell D, Käs J, Ulvick S, Bilby C. 2005. Optical deformability as an inherent cell marker for testing malignant transformation and metastatic competence. *Biophys J*. **88**: 3689-98.

Hartman MA, Spudich JA. 2012. The myosin superfamily at a glance. *J Cell Sci*. **125**: 1627-32. Review.

Holmes KC, Geeves MA. 2000. The structural basis of muscle contraction. *Philos Trans R Soc Lond B Biol Sci*. **355**: 419-31. Review.

Heu C, Berquand A, Elie-Caille C, Nicod L. 2012. Glyphosate-induced stiffening of HaCaT keratinocytes, a Peak Force Tapping study on living cells. *J Struct Biol*. **178**: 1-7.

Hirono M, Denis CS, Richardson GP, Gillespie PG. 2004. Hair cells require phosphatidylinositol 4,5-bisphosphate for mechanical transduction and adaptation. *Neuron*. **44**: 309-20.

Hofmann WA, Vargas GM, Ramchandran R, Stojiljkovic L, Goodrich JA, de Lanerolle P. 2006. Nuclear myosin I is necessary for the formation of the first phosphodiester bond during transcription initiation by RNA polymerase II. *J Cell Biochem*. **99**: 1001-9.

Hofmann WA, Richards TA, de Lanerolle P. 2009. Ancient animal ancestry for nuclear myosin. *J Cell Sci*. **122**: 636-43.

Hokanson DE, Laakso JM, Lin T, Sept D, Ostap EM. 2006a. Myo1c binds phosphoinositides through a putative pleckstrin homology domain. *Mol Biol Cell.* **17**: 4856-65.

Hokanson DE, Ostap EM. 2006b. Myo1c binds tightly and specifically to phosphatidylinositol 4,5-bisphosphate and inositol 1,4,5-trisphosphate. *Proc Natl Acad Sci U S A.* **103**: 3118-23.

Holt JR, Corey DP. 2000. Two mechanisms for transducer adaptation in vertebrate hair cells. *Proc Natl Acad Sci U S A.* **97**: 11730-5.

Holt JR, Gillespie SK, Provance DW, Shah K, Shokat KM, Corey DP, Mercer JA, Gillespie PG. 2002. A chemical-genetic strategy implicates myosin-1c in adaptation by hair cells. *Cell.* **108**: 371-81.

Houdusse A, Gaucher JF, Krementsova E, Mui S, Trybus KM, Cohen C. 2006. Crystal structure of apo-calmodulin bound to the first two IQ motifs of myosin V reveals essential recognition features. *Proc Natl Acad Sci U S A*. **103**: 19326-31.

Houk AR, Jilkine A, Mejean CO, Boltyanskiy R, Dufresne ER, Angenent SB, Altschuler SJ, Wu LF, Weiner OD. 2012. Membrane tension maintains cell polarity by confining signals to the leading edge during neutrophil migration. *Cell*. **148**: 175-88.

Hudspeth AJ, Choe Y, Mehta AD, Martin P. 2000. Putting ion channels to work: mechanoelectrical transduction, adaptation, and amplification by hair cells. *Proc Natl Acad Sci U S A*. **97**: 11765-72.

Hudspeth AJ. 2005. How the ear's works work: mechanoelectrical transduction and amplification by hair cells. *C R Biol.* **328**: 155-62. Review.

Huxley AF, Niedergerke R. 1954. Interference microscopy of living muscle fibres. *Nature.* **173**: 971-3.

Huxley H, Hanson J. 1954. Changes in the cross-striations of muscle during contraction and stretch and their structural interpretation. *Nature*. **173**: 973-6.

Ihnatovych I, Migocka-Patrzalek M, Dukh M, Hofmann WA. Identification and characterization of a novel myosin Ic isoform that localizes to the nucleus. 2012. *Cytoskeleton* **69**: 555-65.

Kaemmer SB. 2011. Introduction to Bruker's ScanAsyst and PeakForce Tapping AFM Technology. Bruker *Application Note.* **133**.

Kahle M, Pridalová J, Spacek M, Dzijak R, Hozák P. 2007. Nuclear myosin is ubiquitously expressed and evolutionary conserved in vertebrates. *Histochem Cell Biol.* **127**: 139-48.

Kasas S, Wang X, Hirling H, Marsault R, Huni B, Yersin A, Regazzi R, Grenningloh G, Riederer B, Forrò L, Dietler G, Catsicas S. 2005. Superficial and deep changes of cellular mechanical properties following cytoskeleton disassembly. *Cell Motil Cytoskeleton*. **62**: 124-32.

Kuznetsova TG, Starodubtseva MN, Yegorenkov NI, Chizhik SA, Zhdanov RI. 2007. Atomic force microscopy probing of cell elasticity. Micron. **38**: 824-33.

Laakso JM, Lewis JH, Shuman H, Ostap EM. 2008. Myosin I can act as a molecular force sensor. *Science.* **321**: 133-6.

Leibler S, Huse DA. 1993. Porters versus rowers: a unified stochastic model of motor proteins. *J Cell Biol*. **121**: 1357-68.

Lekka M, Laidler P, Gil D, Lekki J, Stachura Z, Hrynkiewicz AZ. 1999. Elasticity of normal and cancerous human bladder cells studied by scanning force microscopy. *Eur Biophys J*. **28:** 312-6.

Lekka M, Gil D, Pogoda K, Dulińska-Litewka J, Jach R, Gostek J, Klymenko O, Prauzner-Bechcicki S, Stachura Z, Wiltowska-Zuber J, Okoń K, Laidler P. 2012a. Cancer cell detection in tissue sections using AFM. *Arch Biochem Biophys.* **518**: 151-6.

Lekka M, Pogoda K, Gostek J, Klymenko O, Prauzner-Bechcicki S, Wiltowska-Zuber J, Jaczewska J, Lekki J, Stachura Z. 2012b. Cancer cell recognition—mechanical phenotype. *Micron*. **43**: 1259-66.

Li QS, Lee GY, Ong CN, Lim CT. 2008. AFM indentation study of breast cancer cells. *Biochem Biophys Res Commun.* **374**: 609-13.

Lin T, Greenberg MJ, Moore JR, Ostap EM. 2011. A hearing loss-associated myo1c mutation (R156W) decreases the myosin duty ratio and force sensitivity. *Biochemistry*. **50**: 1831-8.

Lymn RW, Taylor EW. 1971. Mechanism of adenosine triphosphate hydrolysis by actomyosin. *Biochemistry*. 10: 4617-24.

Maravillas-Montero JL, Gillespie PG, Patiño-López G, Shaw S, Santos-Argumedo L. 2011. Myosin 1c participates in B cell cytoskeleton rearrangements, is recruited to the immunologic synapse, and contributes to antigen presentation. *J Immunol.* **187**: 3053-63.

Maupin P, Phillips CL, Adelstein RS, Pollard TD. 1994. Differential localization of myosin-II isozymes in human cultured cells and blood cells. *J Cell Sci*. **107**: 3077-90.

McConnell RE, Tyska MJ. 2010. Leveraging the membrane - cytoskeleton interface with myosin-1. *Trends Cell Biol.* **20**: 418-26. Review.

Meyer G, Amer NM. 1988. Novel optical approach to atomic force microscopy. *Appl Phys Lett*. **53**: 1045-47

Nambiar R, McConnell RE, Tyska MJ. 2009. Control of cell membrane tension by myosin-I. *Proc Natl Acad Sci U S A.* **106**: 11972-7.

Nambiar R, McConnell RE, Tyska MJ. 2010. Myosin motor function: the ins and outs of actin-based membrane protrusions. *Cell Mol Life Sci.* **67**: 1239-54. Review.

Nowak G, Pestic-Dragovich L, Hozák P, Philimonenko A, Simerly C, Schatten G, de Lanerolle P. 1997. Evidence for the presence of myosin I in the nucleus. *J Biol Chem.* **272**: 17176-81.

Obrdlik A, Louvet E, Kukalev A, Naschekin D, Kiseleva E, Fahrenkrog B, Percipalle P. 2010. Nuclear myosin 1 is in complex with mature rRNA transcripts and associates with the nuclear pore basket. *FASEB J*. **24**: 146-57.

Odronitz F, Kollmar M. 2007. Drawing the tree of eukaryotic life based on the analysis of 2,269 manually annotated myosins from 328 species. *Genome Biol.* **8**: R196.

Ostap EM, Pollard TD. 1996. Biochemical kinetic characterization of the Acanthamoeba myosin-I ATPase. *J Cell Biol.* **132**: 1053-60.

Park S, Koch D, Cardenas R, Käs J, Shih CK. 2005. Cell motility and local viscoelasticity of fibroblasts. *Biophys J*. **89**: 4330-42.

Percipalle P, Fomproix N, Cavellán E, Voit R, Reimer G, Krüger T, Thyberg J, Scheer U, Grummt I, Farrants AK. 2006. The chromatin remodelling complex WSTF-SNF2h interacts with nuclear myosin 1 and has a role in RNA polymerase I transcription. *EMBO Rep*. **7**: 525-30.

Pestic-Dragovich L, Stojiljkovic L, Philimonenko AA, Nowak G, Ke Y, Settlage RE, Shabanowitz J, Hunt DF, Hozak P, de Lanerolle P. 2000. A myosin I isoform in the nucleus. *Science*. **290**: 337-41.

Philimonenko VV, Zhao J, Iben S, Dingová H, Kyselá K, Kahle M, Zentgraf H, Hofmann WA, de Lanerolle P, Hozák P, Grummt I. 2004. Nuclear actin and myosin I are required for RNA polymerase I transcription. *Nat Cell Biol*. **6**: 1165-72.

Pittenger B, Erina N, Su C. *2011.* Quantitative Mechanical Properties Mapping at the Nanoscale with PeakForce QNM. Bruker *Application Note.* **128**.

Pollard TD, Korn ED. 1973. Acanthamoeba myosin. I. Isolation from Acanthamoeba castellanii of an enzyme similar to muscle myosin. *J Biol Chem.* **248**: 4682-90.

Pollard TD, Doberstein SK, Zot HG. 1991. Myosin-I. *Annu Rev Physiol.* **53**:653-81. Review.

Purcell TJ, Morris C, Spudich JA, Sweeney HL. 2002. Role of the lever arm in the processive stepping of myosin V. *Proc Natl Acad Sci U S A.* **99**: 14159-64.

Raucher D, Sheetz MP. 2000. Cell spreading and lamellipodial extension rate is regulated by membrane tension. *J Cell Biol.* **148**: 127-36.

Remmerbach TW, Wottawah F, Dietrich J, Lincoln B, Wittekind C, Guck J. 2009. Oral cancer diagnosis by mechanical phenotyping. *Cancer Res.* **69**: 1728-32.

Ricci AJ, Crawford AC, Fettiplace R. 2003. Tonotopic variation in the conductance of the hair cell mechanotransducer channel. *Neuron*. **40**: 983-90.

Richards TA, Cavalier-Smith T. 2005. Myosin domain evolution and the primary divergence of eukaryotes. *Nature.* **436**: 1113-8.

Rotsch C, Radmacher M. 2000. Drug-induced changes of cytoskeletal structure and mechanics in fibroblasts: an atomic force microscopy study. *Biophys J.* **78**: 520-35.

Santos NC, Castanho MA. 2004. An overview of the biophysical applications of atomic force microscopy. *Biophys Chem*. **107**: 133-49. Review.

Semiz S, Park JG, Nicoloro SM, Furcinitti P, Zhang C, Chawla A, Leszyk J, Czech MP. 2003. Conventional kinesin KIF5B mediates insulin-stimulated GLUT4 movements on microtubules. *EMBO J*. **22**: 2387-99.

Schietroma C, Yu HY, Wagner MC, Umbach JA, Bement WM, Gundersen CB. 2007. A role for myosin 1e in cortical granule exocytosis in Xenopus oocytes. *J Biol Chem.* **282**: 29504-13.

Sielski NL, Ihnatovych I, Hagen JJ, Hofmann WA. Tissue specific expression of Myosin IC Isoforms. 2014. *BMC Cell Biol.* **15**:8.

Siemankowski RF, Wiseman MO, White HD. 1985. ADP dissociation from actomyosin subfragment 1 is sufficiently slow to limit the unloaded shortening velocity in vertebrate muscle. *Proc Natl Acad Sci U S A.* **82**:658-62.

Sneddon IN, 1965. The relation between load and penetration in the axisymmetric bossiness problem for a punch of arbitrary profile. *International Journal of Engineering Science.* **3**: 47–57.

Sokac AM, Co C, Taunton J, Bement W. 2003. Cdc42-dependent actin polymerization during compensatory endocytosis in Xenopus eggs. *Nat Cell Biol.* **5**: 727-32.

Sokac AM, Schietroma C, Gundersen CB, Bement WM. 2006. Myosin-1c couples assembling actin to membranes to drive compensatory endocytosis. *Dev Cell.* **11**: 629-40.

Stauffer EA, Scarborough JD, Hirono M, Miller ED, Shah K, Mercer JA, Holt JR, Gillespie PG. 2005. Fast adaptation in vestibular hair cells requires myosin-1c activity. *Neuron*. **47**: 541-53.

Syamaladevi DP, Spudich JA, Sowdhamini R. 2012. Structural and functional insights on the Myosin superfamily. *Bioinform Biol Insights*. **6**: 11-21. Review.

Toyoda T, An D, Witczak CA, Koh HJ, Hirshman MF, Fujii N, Goodyear LJ. 2011. Myo1c regulates glucose uptake in mouse skeletal muscle. *J Biol Chem.* **286**: 4133-40.

Uyeda TQ, Abramson PD, Spudich JA. 1996. The neck region of the myosin motor domain acts as a lever arm to generate movement. *Proc Natl Acad Sci U S A.* **93**: 4459-64.

Vale RD. 2003. The molecular motor toolbox for intracellular transport. *Cell.* **112**: 467-80. Review.

Veigel C, Coluccio LM, Jontes JD, Sparrow JC, Milligan RA, Molloy JE. 1999. The motor protein myosin-I produces its working stroke in two steps. *Nature.* **398**: 530-3.

Venit T, Dzijak R, Kalendová A, Kahle M, Rohožková J, Schmidt V, Rülicke T, Rathkolb B, Hans W, Bohla A, Eickelberg O, Stoeger T, Wolf E, Yildirim AÖ, Gailus-Durner V, Fuchs H, de Angelis MH, Hozák P. 2013. Mouse nuclear myosin I knock-out shows interchangeability and redundancy of myosin isoforms in the cell nucleus. *PLoS One.* **8**: e61406.

Wagner MC, Barylko B, Albanesi JP. 1992. Tissue distribution and subcellular localization of mammalian myosin I. *J Cell Biol.* **119**: 163-70.

Wang FS, Liu CW, Diefenbach TJ, Jay DG. 2003. Modeling the role of myosin 1c in neuronal growth cone turning. *Biophys J*. **85**: 3319-28.

Warshaw, D.M., W.H. Guilford, Y. Freyzon, E. Krementsova, K.A. Palmiter, M.J. Tyska, J.E. Baker, and K.M. Trybus. 2000. The light chain binding domain of expressed smooth muscle heavy meromyosin acts as a mechanical lever. *J. Biol. Chem*. **275**: 37167–37172.

Woolner S, Bement WM. 2009. Unconventional myosins acting unconventionally. *Trends Cell Biol*. **19**: 245-52. Review.

Zadro C, Alemanno MS, Bellacchio E, Ficarella R, Donaudy F, Melchionda S, Zelante L, Rabionet R, Hilgert N, Estivill X, Van Camp G, Gasparini P, Carella M. Are MYO1C and MYO1F associated with hearing loss? 2009. *Biochim Biophys Acta.* **1792**: 27-32.

Zhong Q, Inniss D, Kjoller K, Elings VB. 1993. Fractured polymer/silica fiber surface studied by tapping mode atomic force microscopy. *Surface Sci Lett.* **290**. L688-L692.